A THESIS

on

Synthesis and characterization of Tb_2O_3/TiO_2 nanoparticles and their application in dye sensitized solar cells

Submitted in partial fulfillment of requirement

for the award of the Degree of

MASTER OF TECHNOLOGY

IN

MATERIALS AND METALLURGIAL ENGINEERING

Submitted by:

RAJWANT SINGH

Roll No: 601102005

Under the guidance of

Dr. N.K.VERMA

Senior Professor

SCHOOL OF PHYSICS AND MATERIALS SCIENCE

THAPAR UNIVERSITY

PATIALA – 147 004

PUNJAB

JULY 2013

Dedicated to my Parents

CERTIFICATE

This is to certify that the thesis entitled "**Synthesis and characterization of Tb_2O_3/TiO_2 nanoparticles and their application in dye sensitized solar cells**" which is submitted by **Rajwant Singh, Roll no. 601102005** in the partial fulfillment of the requirement for the award degree of **(M.Tech)** in **Materials and Metallurgical Engineering** from the School of Physics and Materials Science, Thapar University, Patiala, is a record of the candidate's own work carried out by him under my supervision and guidance. The matter embodied in this thesis has not been submitted in part or full to any other university or institution for the award of any degree.

(Dr. N. K. Verma)

Senior Professor,

School of Physics & Materials Science

Thapar University, Patiala -147004 (Punjab)

Countersigned by:

(Dr. Kulvir Singh)

Head and Professor,

School of Physics and Materials Science,

Thapar University

Patiala -147 004 (Punjab)

(Dr. S. K. Mohapatra)

Dean, Academic Affairs,

Thapar University

Patiala -147 004 (Punjab)

Dated:

ACKNOWLEDGEMENT

It is matter of immense pleasure to acknowledge my debt to my revered guide ***Dr. N. K. Verma****, Senior Professor, School of Physics and Material Science, Thapar University, Patiala, for his invaluable guidance and meticulous efforts, without which the accomplishment of the task would have never been possible. I am also thankful to him for giving this opportunity to explore into the real nano world. I am much indebted for his benevolent help, appreciation, and co-operation.*

I am particularly thankful to ***Miss Manveen Kaur*** *for their round the clock help and friendliness. I also express my cordial thanks to all the research scholars of Nano Research Lab,* ***Mr. Gurmeet Singh Lotey****,* ***Mr. Jaspal Singh, Miss Lavanya Khanna, Miss Kamaldeep Kaur****,* ***Miss Gitanjali Dhir****, for their ever available guidance and indispensable comments, which helped me to develop and shape this study in the present form. I express my special regards to Dr. Kulvir Singh Professor and Head, School of Physics and Material Sciences, Thapar University, for his ever-helping attitude during the course of this project work. I thank to all the faculty members and my friends for their help and motivation.*

I would like to express my deepest gratitude to my parents, without whom I am nothing, to provide me great opportunities, everlasting support, big encouragement and lots of love.

Last, but not least, I thank **God** *for giving me strength to overcome difficulty, which crossed my way to be a pole star.*

(Rajwant Singh)

(Roll no. 601102005)

July, 2013

Place: Thapar University, Patiala

ABSTRACT

Surface coating of TiO_2 nanoparticles with Tb_2O_3 has been carried out using sol-gel and hydrothermal method. X-ray diffraction (XRD) analysis reveals the formation of anatase phase TiO_2 nanoparticles. Energy dispersive x-ray spectroscopy (EDAX) shows the presence of Tb_2O_3 on the surface of TiO_2 nanoparticles. Transmission electron microscopy (TEM) confirms the coating of Tb_2O_3 on the TiO_2 nanoparticles surface. The strong quenching in photoluminescence emission, in case of Tb_2O_3/TiO_2 nanoparticles as compared to TiO_2 nanoparticles, has been attributed to the decrease in recombination rate of photo-generated electron–hole pairs. The synthesized nanoparticles have been employed as a photo-anode in DSSCs. From the dye desorption study, it has been revealed that ccompared to TiO_2 electrodes, Tb_2O_3/TiO_2 electrodes adsorbed more dye. The photoelectrochemical property of the Tb_2O_3/TiO_2 based DSSC has been found to improve as compared to bare TiO_2 based DSSC, and the energy conversion efficiency increases from 1.54% to 1.88% under the illumination of simulated light of 100 mW/cm^2. Tb_2O_3 coating played a significant role in minimizing electron-hole recombination which occurred at TiO_2 surface by trapping electrons and facilitating them to anode.

Contents

List of Figures

List of Tables

1.1 Need of solar energy

Solar energy is one of the most promising future energy resources in concern to the sustenance of life on Earth and the depletion of fossil fuels [1]. Perhaps the largest challenge for our global society is to find ways to replace the slowly but inevitably vanishing fossil fuel supplies by renewable resources and, at the same time, avoid negative effects from the current energy system on climate, environment, and health. The quality of human life to a large degree depends upon the availability of clean energy sources. The world-wide power consumption is expected to double in the next 3 decades because of the increase in world population and the rising demand of energy in the developing countries. This implies enhanced depletion of fossil fuel reserves, leading to further aggravation of the environmental pollution [2].

Between 80% and 85% of our energy comes from fossil fuels, a product of ancient biomass stored beneath Earth’s surface for up to 200 million years. Fossil-fuel resources are of finite extent and are distributed unevenly beneath Earth’s surface. When fossil fuels are turned into useful energy though combustion, they produce greenhouse gases and other harmful environmental pollutants. It is projected that the fossil fuel related CO_2 emissions will rise to 42 billion metric tons till year 2035 (Energy Information Administration - EIA, 2010). This enormous amount of CO_2 emission will lead to a severe climatic change of the world and leading to a great anxiety for the scientific era of 21st century [1]. In contrast, solar photons are effectively inexhaustible and unrestricted by geopolitical boundaries. Their direct use for energy production does not threaten health or climate. The solar resource’s magnitude, wide availability, versatility, and benign effect on the environment and climate make it an appealing energy source [3]. This rigorous apprehension leads the scientist for the development of solar cells that utilizes solar energy, a renewable and carbon free energy source. The solar energy strike to the earth in one hour is about 4.3×10^{20} J, which is higher than all the energy consumed in the planet (4.1×10^{20} J). Therefore, covering 0.1% of the earth’s surfaces with solar cell of 10% efficiency would satisfy the current energy demand (Gratzel, 2001) [1]. However, capturing solar energy and converting it to electricity or chemical fuels, such as hydrogen, at low cost and using abundantly available raw materials remains a huge challenge. Chemistry is expected to make pivotal contributions to identify environmentally friendly solutions to this energy problem [2].

The impressive supply of solar energy is complemented by its versatility, as illustrated in figure 1.1. Sunlight can be converted into electricity by exciting electrons in a solar cell. It can yield chemical fuel via natural photosynthesis in green plants or artificial photosynthesis in human-engineered systems. Concentrated or unconcentrated sunlight can produce heat for direct use or further conversion to electricity.

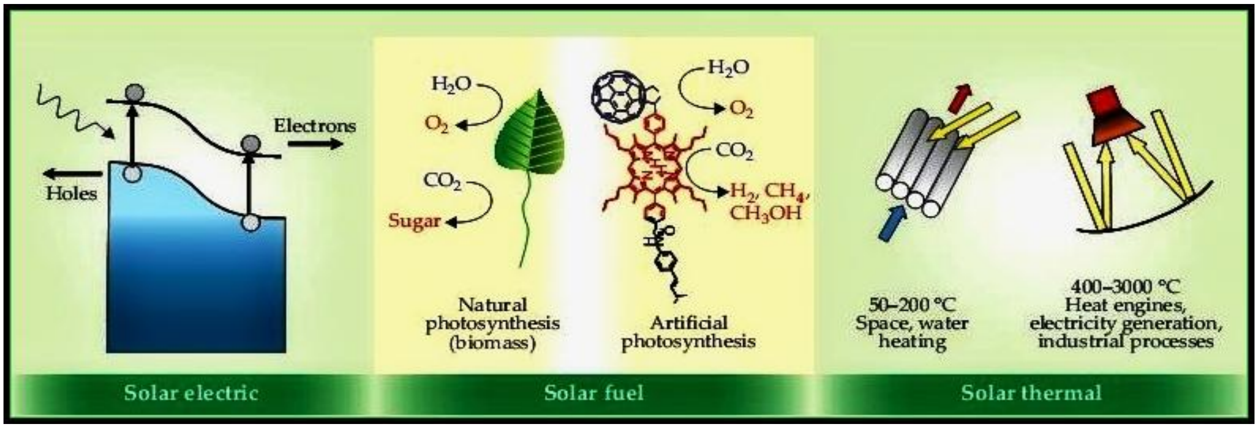

Figure 1.1: Solar photons convert into three forms of energy—electricity, chemical fuel, and heat

Despite the enormous energy flux supplied by the Sun, only a tiny fraction can be utilized for our current and future energy needs. As harvesting electricity from solar energy is very costly; between 5-10 times the electricity costs from fossil fuels, it supplies just 0.015% of the world's electricity demand. Solar fuel, in the form of biomass, accounts for approximately 11% of world fuel use, but the majority of that is harvested unsustainably. Solar heat provides 0.3% of the energy used for heating space and water. The utilization gap between solar energy's potential and our use of it can be overcome by raising the efficiency of the conversion processes [3].

1.2 Brief about generations of solar cells

Solar cells are usually divided into three main categories called generations. The first generation contains solar cells that are relatively expensive to produce, and have a low efficiency. The second generation contains types of solar cells that have an even lower efficiency, but are economical, such that the cost per watt is lower than in first generation cells. The third generation solar cells are very efficient and are not yet commercial, but there is a lot of research going on in this area [4]. Following are the three generations of solar cells:

1.2.1 First-generation solar cells are fully commercial. They use the wafer-based crystalline silicon (c-Si) technology, either single crystalline (sc-Si) or multi-crystalline (mc-Si) [5].

The first modern PV solar cells, silicon (Si) p-n, were developed by Chapin et al. at Bell Laboratories in 1954 [6]. A few years later; they were already intensively used in space exploration. Si cells were the perfect solution for space energy production. Since, apart from regular use in power calculators, traffic signs, clocks and other small appliances, the use of solar cells has grown quite slowly although steadily .

Multi and polycrystalline silicon (mc–Si and pc–Si, respectively) solar cells have dominated the terrestrial PV market. Silicon is far from being the ideal material for PV conversion [7]. The major reason for c–Si market dominance – besides Si natural abundance, low toxicity and a well-established processing technology – is that manufacturers have been supplied with rejected material from the high-tech semiconductor industry. The first amorphous Si cell (a–Si) appeared in 1976 [8]. It is odd that the main competitor to c–Si is also Si-based, especially as a–Si is very different from c–Si. Particularly, a–Si has a high absorption rate and therefore does not need a Si layer as thick as c–Si, which makes it a thin-film technology.

1.2.2 Second-generation solar cells are based on thin-film PV technologies and generally include three main families: 1) amorphous (a-Si) and micromorph silicon (a-Si/µc-Si); 2) Cadmium-Telluride (CdTe); and 3) Copper-Indium-Selenide (CIS) and Copper-Indium-Gallium-Diselenide (CIGS) [5].

Most other PV technologies have the same working principle as c–Si. They are all based in one or more p–n junctions to absorb photons. Polycrystalline CdTe was one of the first PV thin-film materials proposed [9], CdTe solar cells are typically hetero-junctions with CdS being the n-type component. CdTe has the adequate energy band gap (E_g) of 1.45 eV and a high optical absorption coefficient. A troubling issue concerning these cells is CdTe toxicity [10, 11]. The first chalcopyrite solar cells were based on $CuInSe_2$ (CIS), [12] but it was realized later that incorporating Ga to produce $CuInGaSe_2$ (CIGS) results in a widened Eg of 1.3 eV [13]. CIGS solar cells together with a–Si and CdTe are the leading thin-film technologies. Of these three, CIGS cells confirmed maximum efficiency of 19.2% [14].

Although not as much of concern as CdTe, CIGS have some inherent toxicity that may turn out to be a problem for mass production [10]. III–V semiconductor solar cells are very efficient but expensive devices, normally based on GaAs and InGaP, they can be used alone although better results are obtained in tandem cells (multijunction cells) with semiconductors showing different energy bandgaps, thus taking better advantage of the whole solar spectrum. Double and triple junction devices are currently being commercialized; the most common 3J is GaInP/GaAs/Ge with a record efficiency of 32% [14]. In space applications, where cost is not the major problem, multijunction cells have replaced Si cells.

1.2.3 Third-generation solar cells include organic and dye sensitized solar cells (DSSCs) and are still under demonstration and have not yet been widely commercialized [5].

Molecular and polymer organic solar cells are simple PV devices that are made by organic semiconductors ‘‘sandwiched’’ between two electrodes. These cells are characterized by high optical absorption coefficients and low manufacturing costs. A great deal of attention has been given to these cells in recent times, as they are expected to play a key role in the future PV market, particularly now that the 5% efficiency barrier has been overcome [15,16].

They are inexpensive, but not very efficient. In addition to the low efficiency, a major challenge for organic solar cells is their instability over time. Organic cells can be applied to plastic sheets in a manner similar to the printing and coating industries, meaning that organic solar cells are lightweight and flexible, making them ideal for mobile applications and for fitting to a variety of uneven surfaces. Potential uses include battery chargers for mobile phones, laptops, radios, flashlights, toys and almost any hand-held device that uses a battery. PV modules attractive for building-integrated applications as it will expand the range of shapes and forms where PV systems can be applied. Another advantage is that the technology uses abundant, non-toxic materials and is based on a very scalable production process with high productivity [5].

Dye-sensitized solar cells use photo-electrochemical solar cells, which are based on semiconductor structures formed between a photosensitized anode and an electrolyte. In a typical

DSSC, the semiconductor nanocrystals serve as antennae that harvest the sunlight (photons) and the dye molecule is responsible for the charge separation (photocurrent). It is unique in that it mimics natural photosynthesis (Grätzel, 1991). These cells are attractive because they use low-cost materials and are simple to manufacture [5].

Dye-sensitized solar cells (DSSC) are very promising alternative for low cost production of energy. State of the art DSSCs achieve more than 11% energy conversion allied to good performance under any atmospheric condition and low irradiance [17]. The third generation solar cells can be manufactured using solution-based, low-temperature roll-to-roll manufacturing methods, incorporating conventional printing techniques on flexible substrates, which presents the opportunity for a more economical alternative for solar cells within the next few years. The low-cost third generation solar cells will offer larger surface areas with enhanced performance. However, to enable the commercialization of DSSC and OPV in grid-connected or stand-alone rooftop applications, significant progress in cell efficiency, stability, and lifetime are needed. The manufacture of multi-colored cells is truly a competitive advantage of DSSCs. This is achieved by changing the dye, either organic [18] or inorganic [19].

DSSCs main advantages can be summarized as follows:

- Good performance under standard reporting conditions
- Stable performance at non standard conditions of temperature, irradiation and solar incidence angle
- Low cost
- Available environmental-friendly raw materials
- Semi-transparency and multi-color range possibilities

1.3 Dye-sensitized solar cells

The famous 1991 Nature paper by O‘Regan and Gratzel took the scientific community by storm, in which the authors successfully showed the workings of a dye-sensitized photoelectrochemical solar cell with high efficiencies never seen before [20]. The basic principle of the dye-sensitized solar cell (DSSC) rests on the dual function of light harvesting by an organic dye, and charge transport through a semiconductor oxide matrix. The system crucially also incorporates a redox electrolyte, which helps to regenerate the dye. Apart from these crucial components, a DSSC further incorporates a transparent and conducting front electrode, together with a highly conducting counter or back-electrode.

Since the initial work by the Gratzel group, a wealth of DSSC components and configurations has been developed. A staggering number of dyes and electrolyte systems have been investigated, together with numerous types of mesoporous semiconductor oxide films with different morphologies and compositions. After more than 15 years of intense research, still the physical chemistry of several of the basic operations in the DSSC device remains far from fully understood. With time, the chemical complexity of DSSCs has become clear, and the main challenge for future research is to understand and master this complexity, especially at the oxide/dye/electrolyte interface [21].

1.3.1 Mechanism of DSSC

DSSCs are constructed in a sandwich configuration, as shown in Figure 1.2. The DSSCs consist of dye molecule coated to a wide bandgap semiconductor layer, electrolyte, and transparent conduction oxide (TCO) film. The working electrode is nanocrystalline semiconductor deposited onto a TCO. In contrast to the conventional systems where the semiconductor assumes both the task of light absorption and charge carrier transport are separated here. Light is absorbed by a sensitizer, which is bound to the surface of a wide band gap semiconductor; primarily TiO_2, ZnO, and SnO_2 are the preferred compounds. Charge separation takes place at the interface between semiconductor and sensitizer via photoinduced electron injection from the dye into the conduction band of the solid which prevents electron-hole recombination. Carriers are transported in the conduction band of the semiconductor to the charge collector, usually the TCO [22]. The nanocrystalline film has mesoscopic pores that are filled by a mediator such as a redox couple. The photosensitive dye is chemisorbed onto the semiconductor surface in order to capture the light. The counter electrode (CE) is made of TCO coated glass, pre sputtered with thin layer of platinum to catalyze the regeneration process of the redox couple. The maximum output voltage is the difference between Fermi energy of the semiconductor film and the redox potential of the electrolyte [23].

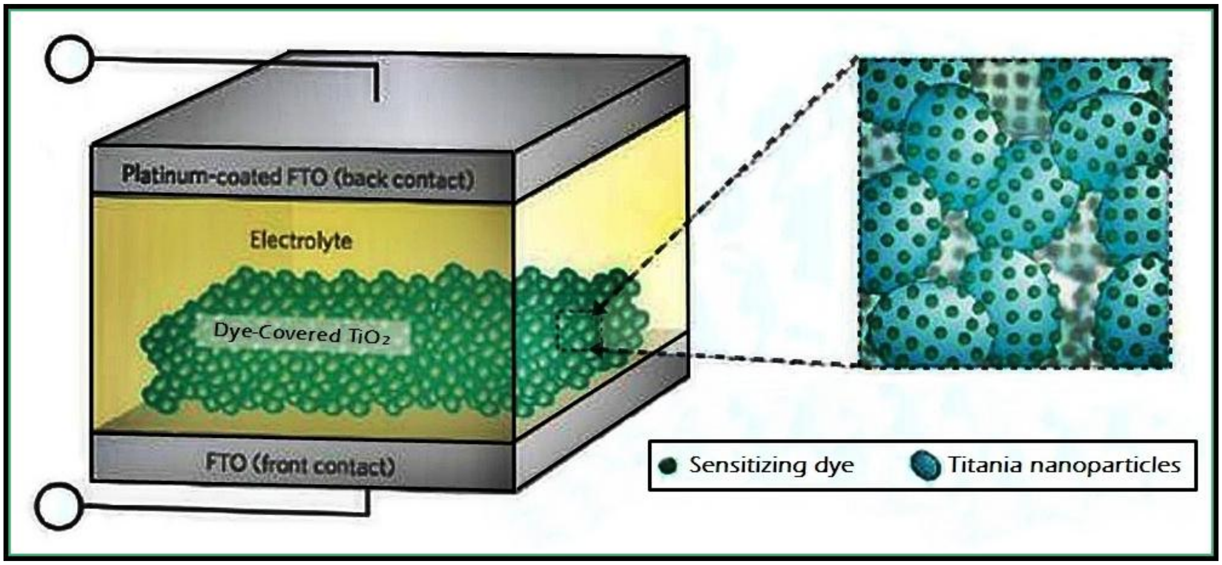

Figure 1.2: The sandwich configuration of a dye sensitized solar cell

The working principle behind the DSSC operation is as follows. As light is illuminated onto the cell, a photon is absorbed by a dye molecule by which the dye is energetically promoted to its excited state. Photoexcitation results in an ultrafast injection of an electron into the conduction band of the semiconductor due to difference in energy levels, producing an oxidized dye. The counter electrode (CE) acts as an electron carrier from the external circuit to the redox electrolyte. The electron then transports through the network of semiconductor (TiO_2 or ZnO) to the collecting anode where it flows into the external circuit allowing energy utilization by a load. Simultaneously, the oxidized dye is reduce to its ground state by the redox species present in the electrolyte, which is usually an iodide (I^-)/triiodide(I_3^-). Iodide reduces the oxidized dye to form an intermediate ionic species (such as I_2^-), that then disproportionates to form triiodide and diffuses to the counter-electrode, providing two electrons per molecule, as shown in figure 1.3. The regeneration cycle of iodide by triiodide takes place at the platinum catalysts-coated cathode. The slow recombination and relatively fast dye regeneration rates of the I^-/I_3^- redox couple have resulted in near unity internal quantum efficiencies for a large number of dyes, providing the high external quantum efficiencies [24].

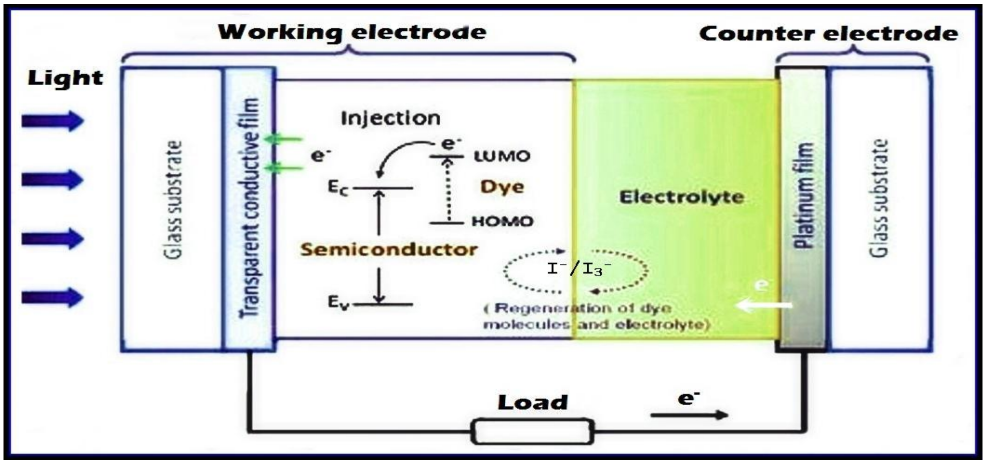

Figure 1.3: Dye-sensitized solar cell device schematic and operation

Overall, this system generated electron power from sunlight without exhibiting any permanent chemical changes, allowing for DSSC to be practical source of renewable energy.

1.4 Review of Literature

Upon illumination of a DSSC, an electron is injected from the dye into the semiconductor film followed by a hole transfer to the electrolyte. The injected electrons must cross the semiconductor film and reach the conducting substrate, while the oxidized ions diffuse towards the back electrode where they are re-reduced [25]. But, the porous geometry and high surface area of photoelectrode, increases the probability of recombination between the injected electrons and the holes in the electrolyte solution, which leads to reduction in efficiency of DSSC [26]. Recombination in DSSCs relates to the reaction of the photoinjected electrons, located in the electron-selective material contacting the dye (the TiO_2), with electron acceptors such as oxidized ions and electron scavengers, located in the hole-selective phase (electrolyte) or the oxidized dye molecules at the interface between the two phases. Three electron acceptors can participate in the recombination process: the oxidized dye molecules, oxidized electrolyte species, and electron scavenger contaminants in the system. The latter may be relevant to the initial operation of the cell, after which they will be fully consumed, unless the electrochemical reaction is fully reversible. No effect on the cell is expected because of the large redox ion concentration [27]. These processes decrease the cell performance by affecting all cell parameters (i.e., open circuit voltage (*V*oc), short-circuit current (*J*sc), and fill factor (FF)).

Different approaches to enhance efficiency and to reduce electron–hole recombination rate have been used such as fabrication of bilayer electrode, preparation of composite semiconductor electrode, and passivation of semiconductor electrode using electro-polymerization method. Kim et al. [26] suggested that coating on the surface of nanoparticles acts as an energy barrier at the electrode–electrolyte interface which reduces this interfacial recombination process [Kim et al.]. Various wide band gap materials such as $CaCO_3$, Al_2O_3, MgO and rare earth oxides have been used as coatings on semiconductor oxides (ZnO, TiO_2); this considerably enhances the efficiency of DSSCs by reducing the recombination rate [28–29]. Among the above-mentioned materials, rare-earth oxides have aroused extensive interest and research due to their specific 4f electronic structure, high band gap and unique photo-electro and magneto properties [30]. The rare earth oxide layer forms energy barrier on nanoparticles, which effectively inhibits the surface charge recombination and improves the energy conversion efficiency of the DSSCs. The dye adsorption and light harvesting capability of electrodes are also increased by coating of rare earth oxides, which enhances the photocurrent density and the open-circuit voltage of the DSSCs. Rare earth oxide coupled with ZnO induces energy band bending in the junction region which facilitates its photoactivity under visible light irradiation. This has been a motivation for the present work.

Li et al. [31] introduced $Gd_2O_3:Sm^{3+}$ nanoparticles in to the TiO_2 film in dye sensitized solar cell. $Gd_2O_3:Sm^{3+}$, acts as a luminescence medium, which improves light harvest via down shift luminescence process and increases photocurrent; $Gd_2O_3:Sm^{3+}$, as a p-type dopant, elevates the energy level of the oxide film and increases the photovoltage. Under simulated solar light irradiation of 100 $mWcm^{-2}$, the solar cell doped $Gd_2O_3:Sm^{3+}$ (6 wt% in doping layer) achieves a light-to electric energy conversion efficiency of 6.72%, which is increased by 12.6% compared with a solar cell without $Gd_2O_3:Sm^{3+}$.

Wu et al. [32] demonstrate the improvement in the photoelectric performance of DSSC by introducing $Y_2O_3:Eu^{3+}$ into the TiO_2 electrode. As a luminescence medium, $Y_2O_3:Eu^{3+}$ improves both the light harvest and the photocurrent. Also being a p-type dopant, $Y_2O_3:Eu^{3+}$ elevates both the energy level of oxide film and the photovoltage of DSSC. With 3 wt.% of $Y_2O_3:Eu^{3+}$ dopant in the TiO_2 electrode, the light-to-electric conversion efficiency of the DSSC reaches 6.52% under a simulated solar light irradiation of $100 mWcm^{-2}$, which is enhanced by a factor of 1.14 compared to that of the DSSC without Y_2O_3:Eu^{3+} doping. This finding demonstrates the feasibility of the conversion luminescence with p-type doping in a dye-sensitized solar cell and provides an effective way to improve the sunlight conversion efficiency for solar cells.

Two lanthanide complexes with pyridine-2, 6-dicarboxylic acid ligands have been synthesized by Wang et al. [33] under hydrothermal or solvothermal conditions. Both nine-coordinate lanthanide metal complexes were attached to a nanocrystalline TiO_2 film to assemble co-sensitized photoelectrodes with N719 for dye-sensitized solar cells, which yielded a remarkably high optoelectronic efficiency of 4.91%. Moreover, the Voc and Isc increased after introducing the cosensitizers.

Xie et al. [34] introduced Y_2O_3:(Eu^{3+}, Gd^{3+}) into the TiO_2 film electrode in DSSC. As a luminescence medium, Y_2O_3:(Eu^{3+}, Gd^{3+}) improves the light harvest via a conversion luminescence process and increases the photocurrent as a p-type dopant, Y_2O_3: (Eu^{3+}, Gd^{3+}) elevates the energy level of oxide film and heightens photovoltage. Under an optimized condition, the cell's light-to-electric conversion efficiency enhances 18.6% compared to the cell without Y_2O_3: (Eu^{3+}, Gd^{3+}) doping. The present result first demonstrates the feasibility of the doping rare-earth oxide in dye-sensitized solar cell and provides an effective way to improve the sunlight conversion efficiency for the solar cell.

Lu et al. [35] fabricated DSSC using porous ZnO film electrodes. The experiment results show that the kinetic parameters for the recombination reactions in the ZnO-based solar cells show different changing trends after modification with the rare earth ions. Generally, it can be ascribed to the different distribution of rare earth ions, which affect the crystallinity, crystal growth and microstructure of the electrode, and then consequentially its surface and electronic properties. Moreover, the rare earth oxides loaded on the electrode surfaces form energy barrier, and effectively suppress the electron recombination and enhance the photovoltage and fill factor; whereas some rare earth ion modifications can passivate the surface states of electrodes. Among the five rare earth ions tested, the Gd-ion modified ZnO film shows an enhanced photocurrent while the La-, Ce-, Nd- and Sm-ion modified films lead to a decreased photocurrent. As a result, the La-, Ce- and Nd-ion modified ZnO-based cells show lower efficiencies than the unmodified one, whereas the optimal conversion efficiency is obtained from the Gd-ion modified ZnO-based cell, with a 44.5% improvement in the efficiency as compared to the unmodified one, indicating this rare earth ion modification is promising in DSSC.

Yahav et al. [36] demonstrated that a La treatment of mesoporous TiO_2 films leads to strong improvements of the photocurrent or photovoltage, depending on the pH of the deposition conditions. At neutral pH, a strong increase in the photovoltage is observed while the photocurrent is reduced. The charge extraction and lifetime measurements indicate that the Voc increase is due to a shell formation around the TiO_2 nanocrystals, generating an interface dipole that shifts the TiO_2 energy bands toward the vacuum level, whereas the reduced photocurrent is caused by less favorable electron injection through the shell. With acidic La treatment, they observe an increase in accumulated electrons in the mesoporous electrode under illumination leading to a strong photocurrent enhancement and attributed this to a higher surface density of adsorbed dye molecules to the TiO_2 nanocrystals. Similar to $TiCl_4$-treated samples, their results suggest that the TiO_2 energy levels are shifted downward while the electron lifetime as a function of accumulated charge increases such that the photovoltage remains nearly unchanged. Finally, they demonstrated that the addition of La acetate to the $TiCl_4$ treatment improves the photovoltaic performance much stronger compared with the well-known La-free $TiCl_4$ procedure.

La_2O_3-modified TiO_2 nanoporous photoanodes were fabricated by Yu et al. [37] for dye-sensitized solar cells by a dip-coating method using an organic lanthanum solution. They concluded that the formation of coordination bonding between the lanthanide ions and dye molecules enhances the dye adsorption. Moreover, photoelectrochemical characterization results demonstrate that the modified photoanodes possess lower electron transfer resistance than the original TiO_2 photoanodes, which alleviates the electron recombination rate. The XRD and XPS analyses suggest the presence of La^{3+} in the modified photoanodes. Consequently, the overall energy conversion efficiency of the La_2O_3 modified DSSCs was dramatically boosted to 9.67% in comparison with 6.84% of the original DSSCs.

Rare earth element cerium was doped in the TiO_2 nanocrystals. The Ce^{4+} and Ce^{3+} oxidized states were formed and highly dispersed in the TiO_2 films. Zhang et al. [38] reported that the cerium ions may exist at grain boundary or on the surface of TiO_2 particles at a high cerium doping amount and decrease the size of the TiO_2 nanocrystal slightly. Cerium with a partially occupied f orbital endowed TiO_2 with special properties. It introduced impurity states under the conduction band edge of TiO_2 and reduced the optical band gap energy even at the low doping amoun0t (<1%). There Ce^{4+} is reduced to Ce^{3+} under electron-injected conditions, making Ce as trap states in the TiO_2 film, which strongly decreased the Jsc and performances of DSSCs with Ce-06 and Ce-09 but enhanced the FF. The optimized performance (7.65%) and Jsc of DSSCs with the Ce-01 photoanode were due to the improved electron injections from the dye.

Zalas et al. [39] studied the electrochemical properties of DSSC fabricated using lanthanide ions (Ce, Yb, Sc, Y, Pr, Sm, Eu, Gd, Dy, and Tm) modified TiO_2 films.

Jian et al. [40] investigated the effect of rare earth oxide Tb_2O_3 additive on transformation behavior and grain growth of anatase and photocatalytic activity for $TiO_2/(O'+\beta')$-Sialon multi-phase ceramic. The added Tb_2O_3 existed in two forms in the catalysts: some entered TiO_2 lattice and the other deposited on the surface of TiO_2. Their results showed that Tb_2O_3 significantly inhibited the transformation process, which displayed an appreciably intensified effect with increasing Tb_2O_3 content. The addition of Tb_2O_3 effectively restrained the grain growth of TiO_2 and the effect became significant with the increase of its content. With the increase of Tb_2O_3 addition, the photocatalytic activity of the catalysts increased and then dropped after reaching the maximum at about 2%. The action mechanism of Tb_2O_3 could be attributed to its optical properties and its effect on phase transformation, grain growth and crystal structure of TiO_2.

Tb_2O_3/TiO_2 nanoparticles have been synthesized by and their optical properties have been investigated [41-43].

But to the best of our knowledge, no report on the synthesis of Tb_2O_3 coated TiO_2 nanoparticles for the application as photo-anode in DSSC has been found in the literature. In the present study, the synthesis of TiO_2 and Tb_2O_3 coated TiO_2 nanoparticles has been done. Structural and optical properties of the synthesized nanoparticles have been investigated and their successful application in DSSCs has been reported.

2.1 Gaps in Research

From the review of literature, it has been found that the following areas are not much explored till now. Following are the gaps in the present study:

- Synthesis of Tb_2O_3 coated TiO_2 nanoparticles.
- Employment of these nanoparticles as photo-anode in DSSC.

2.2 Objectives

I. Synthesis of TiO_2 and Tb_2O_3/TiO_2 nanoparticles.

II. Characterization of synthesized nanoparticles through X-ray diffraction (XRD), Transmission Electron Microscopy (TEM), energy dispersive x-ray spectroscopy (EDAX), photoluminescence (PL), and Fourier Transform Infrared Spectrometer (FTIR).

III. Using the synthesized nanoparticles as photo-anode in DSSC.

2.3 Methodology

Following steps have been taken to achieve the objectives:

- **Synthesis of TiO_2 and Tb_2O_3/TiO_2 nanoparticles:** The synthesis of TiO_2 nanoparticles has been done by sol- gel method, using hydrolysis of titanium isopropoxide. The Tb_2O_3 coating on TiO_2 has been done by hydrothermal treatment.
- **Structural Analysis:** XRD has been done to know about the crystal structure and crystallinity.
- **Morphological study:** The morphology of the synthesized nanoparticles has been examined by TEM.
- **Compositional analysis:** The elements present in the synthesized sample have been detected by EDAX. To know about the bonds present in the synthesized samples, FTIR has been performed.

- **Optical study:** The synthesized samples have been optically characterized through PL. Also, to compare the amount of dye adsorbed on the fabricated electrodes, dye desorption studies have been performed.
- **Fabrication of dye sensitized solar cells:** Using the synthesized nanoparticles, DSSCs have been fabricated by doctor blade technique. The fabricated DSSCs have been characterized by current density-voltage (J-V) characteristics.

3.1 Synthesis of nanomaterials

For synthesis of nanomaterials and the fabrication of nanostructures there are two approaches which are mainly used, they, are top down and bottom up as shown in figure 3.1.

3.1.1 Top down-approach

Top down approach involves slicing or successive cutting of a bulk material to get nano sized particle. Reduction in structure sizes of microscopic elements to the nanometer scale by applying specific machining and etching techniques (e.g. lithography, ultraprecise surface figuring).

Top-down approach includes:

1. High energy milling
2. Chemical mechanical milling
3. Vapour phase condensation
4. Electro-explosion
5. Laser Abilation
6. Sputtering

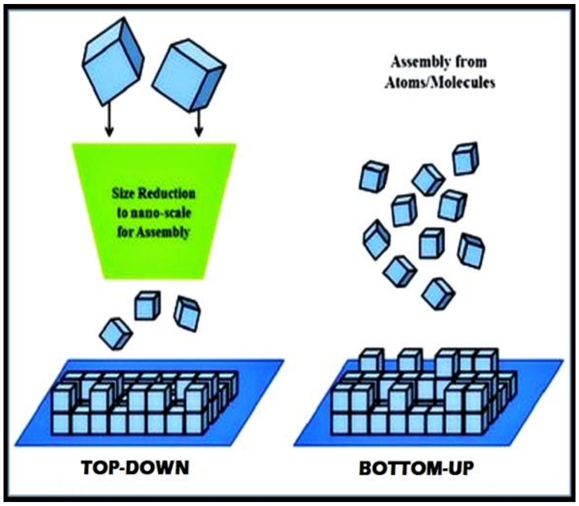

Figure 3.1: Schematic representation of the building up of nanostructures by the two approaches, top down and bottom up

3.1.2 Bottom up-approach

Bottom up approach refers to buildup of a material from the bottom: atom by atom, molecule by molecule or cluster by cluster. It refers to controlled assembly of atomic and molecular aggregates into larger systems (e.g. clusters, organic lattices, supramolecular structures and synthesized macromolecules).

Bottom-up approach includes:

1. Solution combustion method
2. Sol-gel method
3. Hydrothermal Synthesis
4. Micro emulsion
5. Reverse Micelle synthesis
6. Chemical precipitation synthesis

When structures fall into a nanometer scale, there is a little chance for top down approach. All the tools that are used for top down approach are too big to deal with such tiny subjects. Bottom up approach promises a better chance to obtain nano structures with less defects, more homogeneous chemical composition.

3.1.2.1 Sol-gel method

The sol-gel process, as the name implies, involves the evolution of inorganic networks through the formation of a colloidal suspension (sol) and gelation of the sol to form a network in a continuous liquid phase (gel). The precursors for synthesizing these colloids consist usually of a metal or metalloid element surrounded by various reactive ligands. The starting material is processed to form a dispersible oxide and forms a sol in contact with water or dilute acid. Removal of the liquid from the sol yields the gel, and the sol/gel transition controls the particle size and shape. Calcination of the gel produces the oxide. Sol-gel processing refers to the hydrolysis and condensation of alkoxide-based precursors [44]. The reactions involved in the sol-gel chemistry based on the hydrolysis and condensation of metal alkoxides $M(OR)_z$ can be described as follows:

$$\mathbf{MOR + H_2O \rightarrow MOH + ROH\ (hydrolysis)} \qquad \mathbf{(3.1)}$$

$$\mathbf{MOH + ROM \rightarrow M\text{-}O\text{-}M + ROH\ (condensation)} \qquad \mathbf{(3.2)}$$

The sol-gel process can be described by a series of distinct steps:

I. First step involves formation of different stable solutions of the alkoxide or solvated metal precursor (the sol).

II. In the second step gelation starts, resulting from the formation of an oxide- or alcohol-bridged network (the gel) by a polycondensation or polyesterification reaction that results in a dramatic increase in the viscosity of the solution.

III. Third step is aging of the gel (Syneresis), during which the polycondensation reactions continue until the gel transforms into a solid mass, accompanied by contraction of the gel network and expulsion of solvent from gel pores. It is referred to as coarsening, phenomenon by which smaller particles are consumed by larger particles during the growth process and phase transformations may occur concurrently with syneresis.

IV. The fourth step is drying of the gel, when water and other volatile liquids are removed from the gel network. This process is complicated due to fundamental changes in the structure of the gel. The drying process has itself been broken into four distinct steps: (i) the constant rate period, (ii) the critical point, (iii) the falling rate period, and (iv) the second falling rate period.

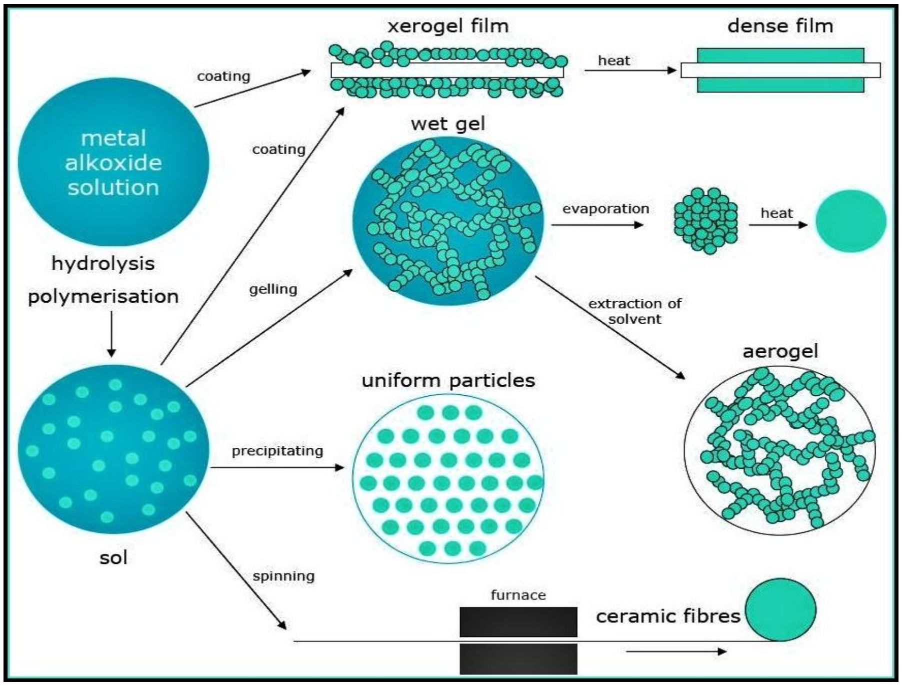

Figure 3.2: Schematic representation of sol-gel process of synthesis of nanomaterials

V. The fifth step involves dehydration, during which surface bound M-OH groups are removed, there by stabilizing the gel against rehydration. This is normally achieved by calcining the monolith at temperatures up to 800^0C.

VI. The sixth step involves densification and decomposition of the gels at high temperatures ($T>800^0$C). The pores of the gel network are collapsed, and remaining organic species are volatilized. The typical steps that are involved in sol-gel processing are shown in the schematic diagram, figure 3.2 [44].

The interest in this synthesis method arises due to the possibility of synthesizing nonmetallic inorganic materials like glasses, glass ceramics or ceramic materials at very low temperatures compared to the high temperature process required by melting glass or firing ceramics.

3.1.2.2 Hydrothermal synthesis

Hydrothermal synthesis refers to the synthesis by chemical reactions of substances in a sealed heated solution above ambient temperature and pressure. Understanding the mechanism of hydrothermal reactions is particularly necessary for both the suitable application of a method to a specific synthesis and the exploration of new materials with desired properties. Basically, the mechanism of hydrothermal reactions follows a liquid nucleation model [45]. It is different from that of solid-state reactions, where the reaction mechanism involves mainly diffusion of atoms or ions at the interface between reactants. New methods and strategies play an important role in the investigation of hydrothermal synthesis. The various methods such as induced growth through crystal seeds, structure-directing agent technique, mineralizing, templating, complexing, non-aqueous solvothermal routes, high temperature and pressure technique, and redox environment control make hydrothermal reactions particularly available for new advanced solid materials.

Hydrothermal synthesis has been successful for the preparation of important solids such as microporous crystals, supersonic conductors, chemical sensors, electronically conducting solids, complex oxide ceramics and fluorides, magnetic materials, and luminescence phosphors. It is also a route to unique condensed materials including nanometer particles, gels, thin films, equilibrium defect solids, distinguished helical and chiral structures, and particularly-stacking-sequence materials [46].

3.2 Synthesis of TiO_2 nanoparticles

The synthesis of TiO_2 nanoparticles was done by sol-gel method. This process consists of hydrolysis and condensation of titanium isopropoxide. Following is the step-wise procedure for the synthesis of TiO_2 nanoparticles:-

- A mixture of 95 ml of distilled water and 150 ml of 2-propanol was made. Second mixture of 21 ml of titanium isopropoxide and 150 ml of 2-propanol was prepared. These two solutions were mixed together.
- The mixture was stirred on a magnetic stirrer for 4 hour.
- The precipitates were collected, filtered, washed several times with water and ethanol.
- After washing, the powder obtained was dried in oven for 24 hour at 60ºC.
- The obtained powder was calcined at 450°C for 30 minutes.

3.3 Synthesis of terbium coated titanium dioxide nanoparticles

After the above synthesis, Tb_2O_3 coating on TiO_2 nanoparticles was performed by hydrothermal technique. Following is the step-wise procedure used:-

- 0.001M of $(Tb(NO_3)_2$ in 18ml of ethanol was reduced with 0.02M of $NaBH_4$, and, added in 0.2M of TiO_2 nanoparticles dispersed in ethanol.
- The solution was stirred on a magnetic stirrer for 10 min.
- Finally, this solution was transferred to autoclave for hydrothermal treatment for 12 hour at 140ºC.
- The so obtained precipitates were filtered, washed and dried at 60ºC.
- Then the obtained particles were calcined at 500ºC for 1 hour (this sample is named as TiTb1).
- Similarly, two more samples were synthesized by adjusting the concentration of $(Tb(NO_3)_2$ to 0.005M and 0.01M (TiTb5 and TiTb10).

3.4 Characterization Techniques

Success in devising and collecting systems on the scale of nanometers require a deeper understanding of the basic processes and phenomena involved. Hence, one of the current key objectives is to adapt and develop a range of techniques that can characterize the structural, electronic, compositional and optical properties of the nanostructured systems [47]. These techniques include x-ray diffraction (XRD), transmission electron microscope (TEM), energy dispersive x-ray spectroscopy (EDAX), Fourier transform infrared spectroscope (FTIR), UV-Visible spectroscopy (UV-Vis) and photoluminescence (PL) study.

3.4.1 X- Ray Diffraction

X-ray diffraction (XRD) is a versatile, non-destructive analytical technique that reveals detailed information about the chemical composition and type of molecular bond of crystalline phase [48]. X-rays are the waves with wavelengths on the order of 0.1 Å to ~10 Å.

3.4.1.1 Generation of X-rays

When electrons strike a metal anode with sufficient energy, X-rays are produced. This process is typically accomplished using a sealed x-ray tube, which consists of a metal target (often copper metal) and a tungsten metal filament, which can be heated by passing a current through it (typically 10-15 mA), resulting in the “boiling off” of electrons from the hot tungsten metal surface. These “hot” electrons are accelerated from the tungsten filament (negative bias) to the metal target (positive bias) by an applied voltage (typically 15-30 kilovolts). The collision between these energetic electrons and electrons in the target atoms results in electron from target atoms being excited out of their core-level orbital’s, placing the atom in a short-lived excited state. The atom returns to its ground state by having electrons from lower binding energy levels (i.e. levels further from the nucleus) make transitions to the empty core levels. The difference in energy between these lower and higher binding energy levels is radiated in the form of X-rays. This process results in the production of characteristic X-rays. Thus X-rays provide a convenient means of determining what elements are present in a sample because of the unique wavelengths produced by each unique element as shown in figure 3.3 [49].

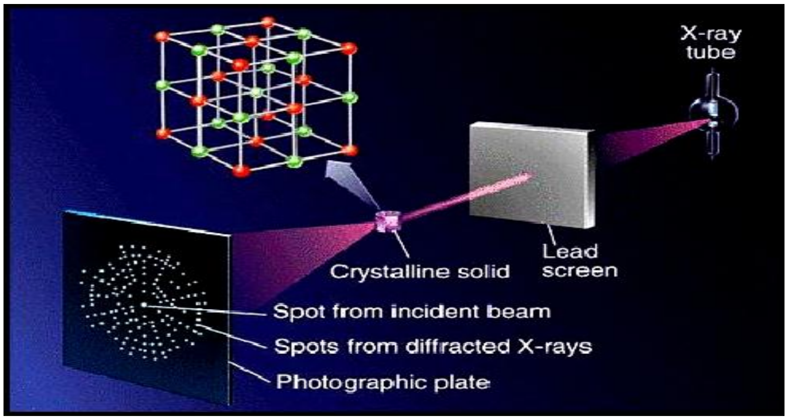

Figure 3.3: Illustration of x-ray diffraction

3.4.1.2 Working principle of XRD

Diffraction is a scattering phenomenon. When X-rays are incident on crystalline solids, they are scattered in all directions. In some of these directions, the scattered beams are completely in phase and reinforce one another to form the diffracted beams. The Bragg law describes the conditions under which this would occur. It is assumed that a perfectly parallel and monochromatic X-ray beam, of wavelength λ, is incident on a crystalline sample at an angle θ as shown in figure 3.4.

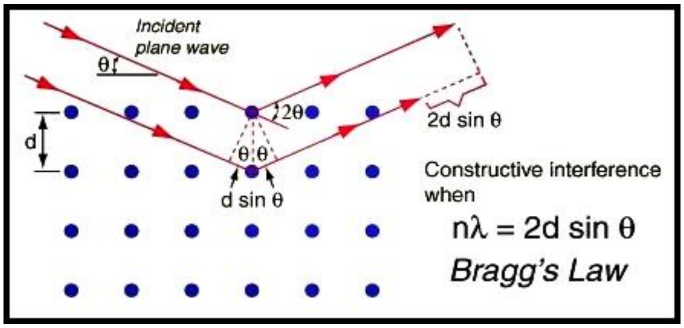

Figure 3.4: Incident x-rays are diffracted by the layers of atoms in a crystalline material

The concept of x-ray diffraction can be described by the Bragg's Law.

Diffraction will occur if:

$$n\lambda = 2d \sin\theta \qquad (3.3)$$

where d is the distance between atomic planes, n an integer, λ the wavelength, and θ the angle of incidence of the x-ray beam and the atomic planes.

$2d \sin\theta$ is the path length difference between two incident x-ray beams where one x-ray beam takes a longer, but parallel, path because it "reflects" off an adjacent atomic plane. This path length difference must equal an integer value of λ of the incident x-ray beams for constructive interference to occur such that a reinforced diffracted beam is produced.

For a given λ of incident x-rays and interplanar spacing, d, in a mineral, only specific θ angles will satisfy the Bragg equation. No "reflections" will occur until the incident beam makes an angle θ that satisfies the Bragg equation with $n = 1$. Continued rotation leads to other "reflections" at higher values of θ and correspond to when $n = 2, 3$ ... etc.; these known as 1st, 2nd, 3rd order, etc., "reflections" [48].

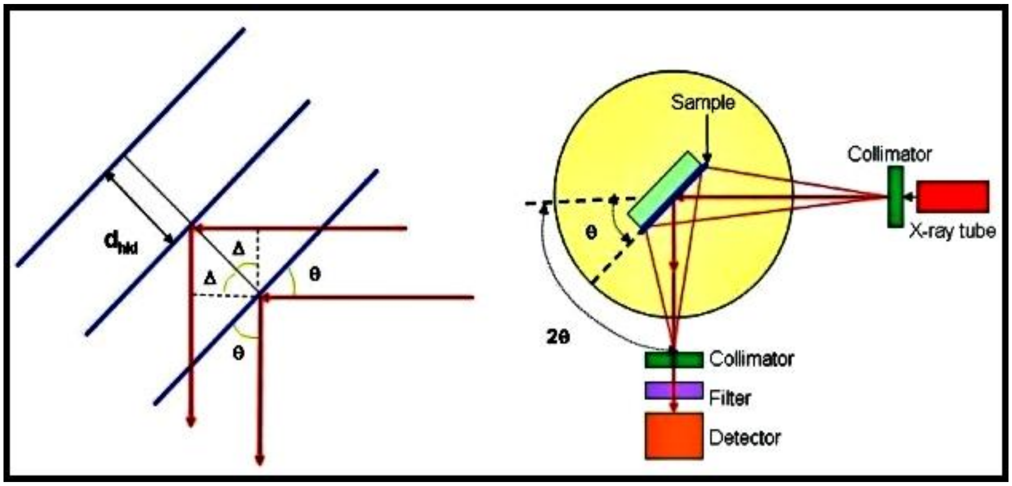

Figure 3.5: Schematic of x-ray diffractometer

In figure 3.5, the blue lines represent planes of atoms in the reciprocal lattice where d_{hkl} is the distance between planes defined by the Miller indices h, k and l. The sample loaded into the system where it is rotated through a chosen 2θ angle. The incident x-ray beam is reflected out of the sample and may go through several slits (collimator and filter) before entering into a detector which registers the intensity at an angle 2θ with respect to the sample plane.

By varying the angle θ, the Bragg's Law conditions are satisfied by different d-spacing in polycrystalline materials. Plotting the angular positions and intensities of the resultant diffracted peaks of radiation produces a pattern, which is characteristic of the sample. Where a mixture of different phases is present, the resulting diffractogram is formed by addition of the individual patterns. Based on the principle of x-ray diffraction, a wealth of structural, physical and chemical information about the material investigated can be obtained.

When an incident beam angle is equal to the angle of reflection, the beams reflected are in phase with each other; that is they have a path difference with an integer number of wavelengths. This condition is referred to as the Bragg diffraction condition. At certain characteristic angles for each material the Bragg diffraction condition will be met and large intensities of the reflected beam will be detected whereas at most 2θ angles small or no intensity of the reflected beam will be detected. These intensities are seen as peaks in a plot of 2θ vs. Intensity. The peak positions, peak shapes and relative intensities are directly correlated to crystallographic spacing, phase, and grain or particle size. Thus XRD spectra can be used to determine various material parameters [50].

3.4.1.3 Ideal Uses of XRD

- Phase identification for a large variety of bulk and thin-film samples
- Detecting crystalline minority phases (at concentrations greater than ~1%)
- Determining crystallite size for polycrystalline films and materials
- Determining percentage of material in crystalline form versus amorphous
- Determining strain and composition in epitaxial thin films
- Measuring residual stress in bulk metals and ceramics [51]

3.4.2 Transmission electron microscopy

Transmission electron microscope (TEM) operates on the same basic principles as the light microscope but uses electrons instead of light. What you can see with a light microscope is limited by the wavelength of light. TEM's use electrons as "light source" and their much lower wavelength make it possible to get a resolution a thousand times better than with a light microscope [52] as shown in figure 3.6.

Objects to the order of a few angstroms (10^{-10} m) can be seen using TEM. For example, study of small details in the cell or different materials down to near atomic levels can be studied. The possibility for high magnifications has made the TEM a valuable tool in both medical, biological and materials research [53].

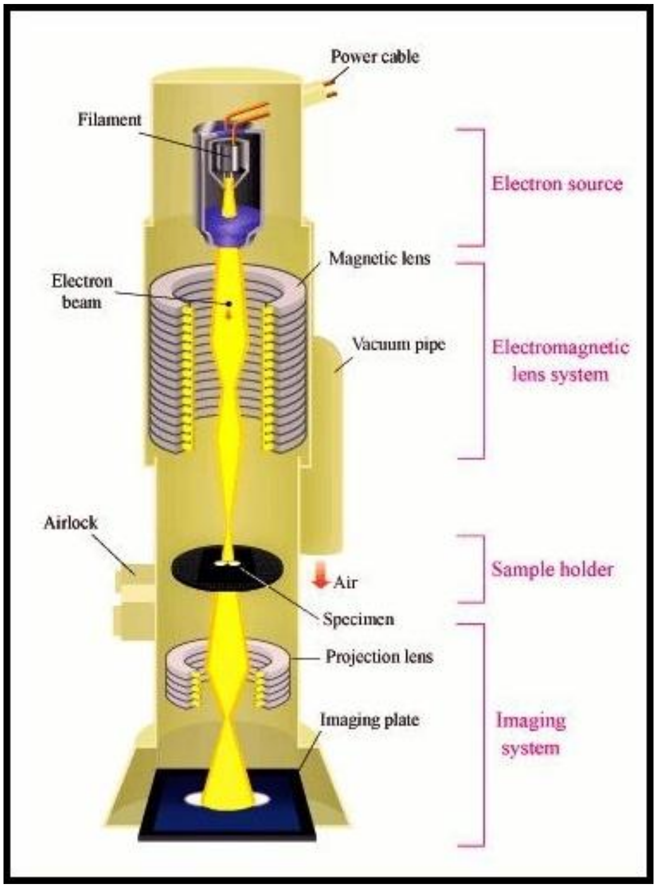

Figure 3.6: Showing a schematic outline of a TEM. A TEM contains four parts: electron source, electromagnetic lens system, sample holder, and imaging system.

3.4.2.1 Main parts of TEM

Electron source

The electron source consists of a cathode and an anode. The cathode is a tungsten filament which emits electrons when being heated. A negative cap confines the electrons into a loosely focused beam. The beam is then accelerated towards the specimen by the positive anode. Electrons at the rim of the beam will fall onto the anode while the others at the center will pass through the small hole of the anode. The electron source works like a cathode ray tube.

Electromagnetic lens system

After leaving the electron source, the electron beam is tightly focused using electromagnetic lens and metal apertures. The system only allows electrons within a small energy range to pass through, so the electrons in the electron beam will have a well-defined energy.

Sample holder

The sample holder is a platform equipped with a mechanical arm for holding the specimen and controlling its position.

Imaging system

TEM uses high energy electrons (up to 300 kV accelerating voltage) which are accelerated to a very high speed. The electron beam behaves like a wavefront with wavelength about a million times shorter than light waves. When an electron beam passes through a thin-section specimen of a material, electrons are scattered. A sophisticated system of electromagnetic lenses focuses the scattered electrons into an image or a diffraction pattern, or a nano-analytical spectrum, depending on the mode of operation [54].

3.4.2.2 Principle of TEM

The basic principles of electron microscopy are identical to those of light microscopy; the main difference is that in electron microscope electromagnetic lenses are used not optical lenses. It also focuses a high velocity electron beam rather than visible light. The electrons are absorbed by atoms in air and that is the reason why the whole tube between the electron source and the viewing screen is sustained beneath an ultrahigh vacuum. The TEM directs a beam of electrons via a specimen. The electrons are emitted by a tungsten cathode whenever it is electrically heated. A condenser lens concentrates the electron beam on to the sample, objective and projects them on to a presentation screen or on a piece of photographic film [55].

Electron beams are not only of particulate nature but also behave as a form of radiation with a defined and much shorter wavelength than light; if an electron beam instead of light beams is used to "illuminate" a specimen, the microscope's resolution R is tremendously increased because the wavelength of an electron beam is with 0.005 nm approximately 100,000-times shorter than an average light beam of about 600 nm [56].

The smallest distance D at which the two objects can be differentiated is proportional to the wavelength λ of the light which illuminates the objects. Therefore the limit of resolution for the electron microscope is hypothetically 0.005 nm or 40,000 times better than the resolution of the light microscope and 2 million times enhanced than that of unaided human eye. However in reality a resolution of 0.10nm can be acquired with TEM, around 2000 times better than the resolution of the light microscopes [55].

3.4.2.3 Ideal uses of TEM

- Identification of nm sized defects on integrated circuits, including embedded particles and residues at the bottom of vias.
- Determination of crystallographic phases as a function of distance from an interface.
- Nanoparticle characterization: Core/shell investigations, agglomeration, effects of annealing.
- Ultra small area elemental maps.
- Crystal defect characterization [57]

3.4.3 Energy Dispersive X-Ray Spectroscopy

Energy Dispersive X-Ray Spectroscopy (EDAX) is a chemical microanalysis technique. The EDAX technique detects x-rays emitted from the sample during bombardment by an electron beam to characterize the elemental composition of the analyzed volume [58].

3.4.3.1 Main parts of EDAX

The EDAX system consists of three main components: an x-ray detector, separated from the SEM chamber by a very thin polymer window; pulse processing circuitry, which determines the energy of the detected x-rays; and analyzer equipment, which interprets the x-ray data and displays it on a computer screen as illustrated in figure 3.7 [59].

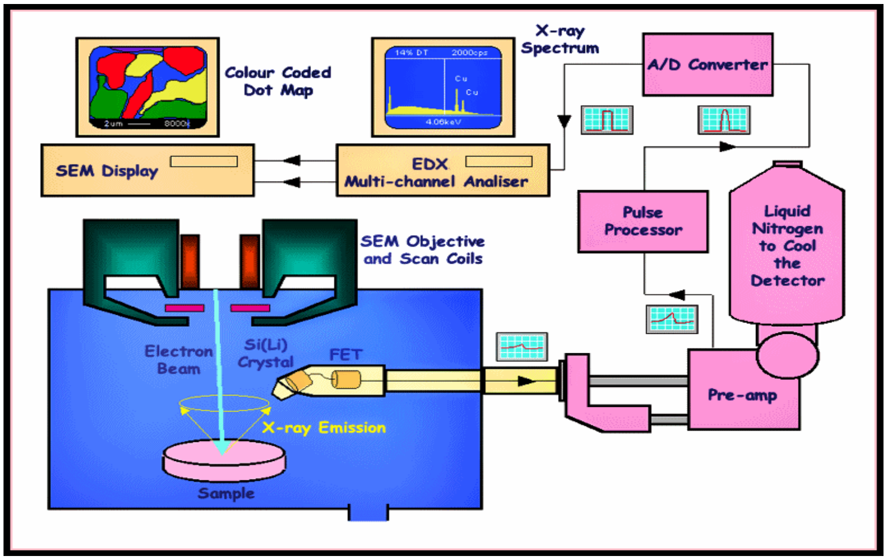

Figure 3.7: X-ray detector schematic

When the sample is bombarded by the electron beam, electrons are ejected from the atoms comprising the sample's surface. The resulting electron vacancies are filled by electrons from a higher state, and an x-ray is emitted to balance the energy difference between the two electron’s states as shown in figure 3.8. The x-ray energy is characteristic of the element from which it was emitted [58].

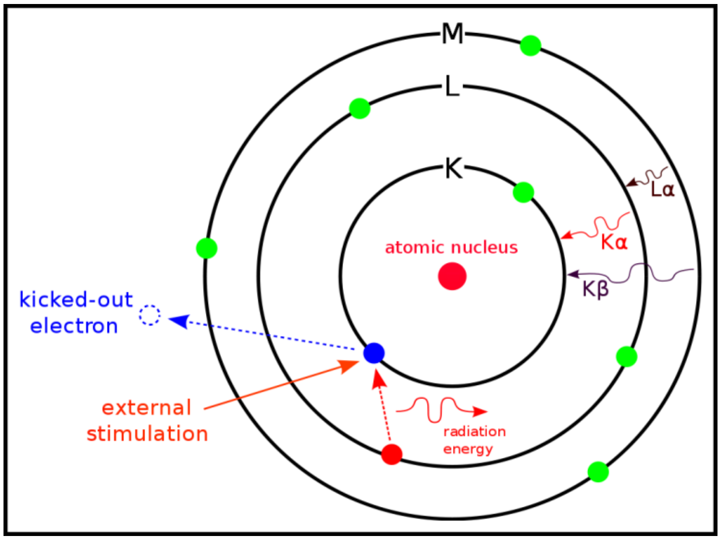

Figure 3.8: In EADX, an incoming X-ray ejects an inner shell electron, leaving a vacancy which is filled by an outer shell electron, releasing a photon

3.4.3.2 Principle of EDAX

The x-ray detector is housed inside a metal tube, which is inserted into the SEM chamber so that the detector is very close to the final aperture of the SEM column, and pointed at the surface of the specimen. Thus, some of the emitted X-rays will pass through the thin polymer window on to the surface of the detector. The detector is a semiconductor made of silicon doped with lithium. This detector must be operated at liquid nitrogen temperatures [59].

When an X-ray strikes the detector, it will generate a photoelectron within the body of the Si. As this photoelectron travels through the Si, it generates electron-hole pairs. The electrons and holes are attracted to opposite ends of the detector with the aid of a strong electric field. The size of the current pulse thus generated depends on the number of electron-hole pairs created, which in turn depends on the energy of the incoming X-ray [60].

The signal is then sent to multichannel analyzer where the pulses are sorted by voltage value. The energy, as determined from the voltage measurement for each incident x-ray, is sent to a computer for display and further data evaluation. The spectrum of x-ray energy versus counts is evaluated to determine the elemental composition of the sampled volume.

3.4.3.3 Ideal uses of EDAX

- Foreign material analysis
- Corrosion evaluation
- Coating or boundary layer composition analysis
- Rapid material alloy identification
- Small component material analysis
- Phase identification and distribution [58]

3.4.4 Fourier Transform Infrared Spectroscopy

Fourier Transform Infrared Spectroscopy (FTIR) is a novel infrared technique used to detect vibrational transitions of a molecule. The advantage of FTIR compared to conventional infrared spectroscopy is that all wavenumbers are measured at once with help of Michelson interferometer [61].

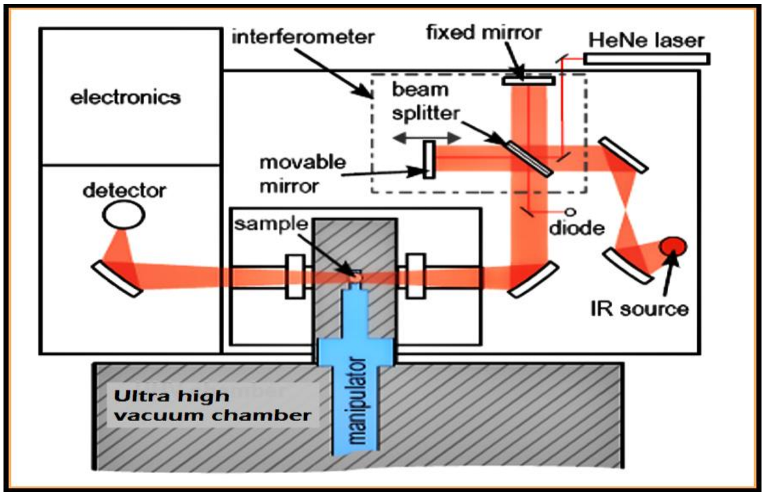

Figure 3.9: Ray diagram of an FTIR spectroscopy

But for the purists, an FTIR is a method of obtaining infrared spectra by first collecting an interferogram of a sample signal using an interferometer as illustrates in figure 3.9, and then performing a Fourier Transform (FT) on the interferogram to obtain the spectrum. An FTIR spectrometer collects and digitizes the interferogram, performs the FT function, and displays the spectrum [62].

3.4.4.1 Working of FTIR

FTIR is a technique that measures the frequency dependence of the interaction of radiation with matter. FTIR is the combined use of IR light, for illuminating a light absorbing sample, with an interferometer, for producing an interference pattern from which an absorption spectrum characteristic of the sample is recovered through Fourier transformation. In FTIR, the selection rules governing band assignments are the same as those found for dispersive IR spectroscopy. The majority of IR spectrometers now use a Michelson interferometer to produce the interference pattern. A typical Michelson interferometer consists of two perpendicular mirrors and a beamsplitter. One of the mirror is a stationary mirror and another one is a movable mirror. Referring to figure 3.10, a collimated beam emanating from an IR light source is split in half by a beam splitter.

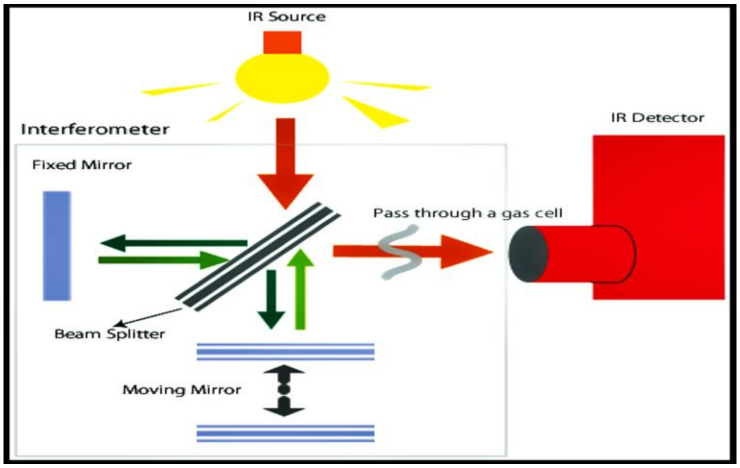

Figure 3.10: Optical illustration of michelson interferometer

The Michelson interferometer is used to split one beam of light into two so that the paths of the two beams are different. Then it recombines the two beams and conducts them into the detector where the differences of the intensity of these two beams are measured as a function of the difference of the paths. The beam-splitter is designed to transmit half of the light and reflect half of the light. Subsequently, the transmitted light and the reflected light strike the stationary mirror and the movable mirror, respectively. When reflected back by the mirrors, two beams of light recombine with each other at the beam-splitter [63].

A computer controls the interferometer, accumulates, stores and manipulates interferogram data, performs the Fourier transformation, as well as post spectral manipulation such as plotting, calibration and correlation. Manipulation of interferogram data consists of co-adding successive scans, apodization and phase correction. The first operation improves the signal-to-noise ratio of a spectrum, whereas the latter two remove instrumental artifacts.

Unlike a dispersive instrument where the light interacting with the sample has a narrowly defined frequency, the interference pattern contains light having a wide range of frequencies covering either the near infrared (NIR) or the mid-infrared (Mid-IR) region of the electromagnetic spectrum. Since the sample absorbs only at certain frequencies, the shape of the interference pattern, or interferogram, changes upon interacting with the sample, thereby producing a spectrum characteristic of the sample [64].

3.4.4.2 Ideal uses of FTIR

- Identifying organic contaminants (e.g. residues)
- Characterization or identification of organic materials (e.g. solids, powders, films, or liquids)

3.4.5 Photoluminescence spectroscopy

Photoluminescence (PL) spectroscopy is a contactless, nondestructive method to probe the electronic structure of materials and is therefore a powerful tool upon studying fundamental properties of semiconductor materials [65]. Typically, a laser beam is absorbed by a sample. Excess energy can be brought to the material removed by light emission or luminescence. As the excitation of the material is produced by a light beam, this luminescence is called "photoluminescence".

In fact, photoluminescence spectroscopy gives only information about the lowest of the studied system energy levels. In semiconductors the most common radiative transition occurs between states of the conduction band states and the valence band separated by an energy difference called bandgap ("gap"). In a PL, excitement is generated by a laser at a much higher energy than the band gap energy. Photo carriers created electrons and holes relax to their respective band edges and recombine to emit light energy "gap" of the semiconductor [66].

3.4.5.1 Principle of PL

The general concept of a PL measurement is easy to grasp as outlined by figure 3.11. Light of energy in excess of the fundamental band gap is directed on a semiconductor sample where it gets absorbed, thereby generating photoelectrons and holes. These carriers release part of their energy by nonradiative processes (mostly through emission of phonons) until they reach a local ground state, from where they may radiatively recombine upon emission of a new photon. The energy of the emitted light, which is called luminescence, relates to the energy difference of the electronic states involved in the transition. The optical polarization may moreover yield valuable information on the symmetry and magnetic properties of the probed material.

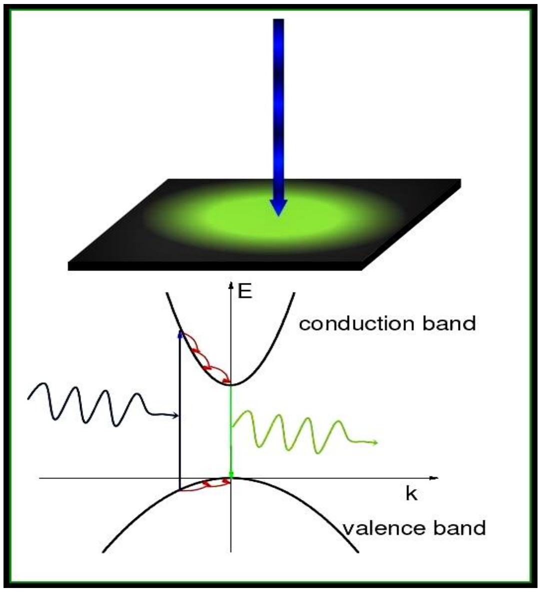

Figure 3.11: Principle of beam of light in PL

PL provides a wealth of information on semiconductor properties such as the fundamental bandgap, impurity levels and defect states, electronic complexes (e.g. excitons) and the relaxation mechanisms of carriers in the material [65].

3.2.5.2 Working of PL

The basic elements of an experimental setup for PL spectroscopy consist of an optical excitation source, a spectrometer and a detector. A typical arrangement is shown in figure 3.12. The excitation laser beam is focused on the sample using a lens of focal length f of the order of typically 20-30 cm. The emitted light can be collected either by a single lens or two lenses F_1 and F_2. The latter configuration allows a lens F_1 of short focal length which improves the efficiency of collection. Moreover, F_2 is selected to have the same optical aperture as the spectrometer, which prevents additional losses [66].

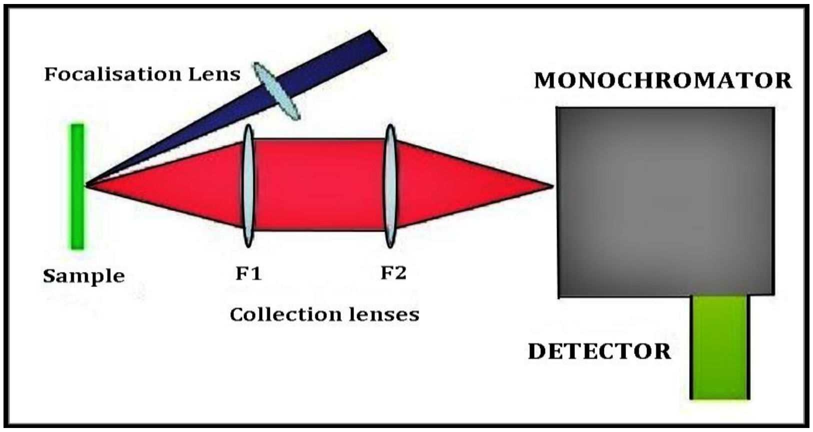

Figure 3.12: Basic diagram of a montage of photoluminescence spectroscopy

3.4.5.3 PL applications and uses:

- **Band gap determination**: The most common radiative transition in semiconductors is between states in the conduction and valence bands -bandgap of a semiconductor. Bandgap determination is particularly useful when working with new compound semiconductors.

- **Impurity levels and defect detection:** Radiative transitions in semiconductors also involve localized defect levels. The PL energy associated with these levels can be used to identify specific defects, and the PL intensity can be used to determine their concentration.

- **Recombination mechanisms:** As discussed above, the return to equilibrium, also known as "recombination" can involve both radiative and nonradiative processes.The PL intensity and its dependence on the level of photo-excitation and temperature are directly related to the dominant recombination process.

- **Material quality**: In general, nonradiative processes are associated with localized defect levels, whose presence is detrimental to material quality and subsequent device performance. Thus, material quality can be measured by quantifying the amount of radiative recombination [67].

3.4.6 UV-Visible Absorption spectroscopy

Ultraviolet-Visible absorption (UV-Vis) spectroscopy is useful to characterize the absorption, transmission, and reflectivity of a variety of compounds and technologically important materials, such as pigments, coatings etc. The UV-Vis spectra have broad features that are of some use for sample identification but are very useful for quantitative measurements [68]. UV-Vis spectrum results from the interaction of electromagnetic radiation in the UV-Vis region with molecules, ions or complexes. It forms the basis of analysis of different substances such as, inorganic, organic and biochemical’s. These determinations find applications in research, industry, clinical laboratories and in the chemical analysis of environmental samples.

3.4.6.1 Principle of UV-VIS Spectroscopy

In order to obtain a UV-VIS spectrum the sample is ideally irradiated with the electromagnetic radiation varied over a range of wavelength. A monochromatic radiation i.e., a radiation of a single wavelength is employed at a time. This process is called scanning [69]. Molecules absorb energy and this energy can bring about translational, rotational or vibrational motion or ionization of the molecules depending upon the frequency of the electromagnetic radiation they receive. Excited molecules are unstable and quickly drop down to ground state again giving off the energy they have received as electromagnetic radiation [68].

The amount of the radiation absorbed at each wavelength is measured and plotted against the wavelength to obtain the spectrum. Thus, a typical UV spectrum is a plot of wavelength or frequency versus the intensity of absorption.

3.4.6.2 Working of UV-VIS Spectroscopy

There are five essential components of UV-VIS instruments. These are: radiation source, wavelength selector, sample holder, detector and a signal processing and output device as shown in figure 3.13. The wavelength selection is achieved by absorption filters in low cost instruments for visible region. In the modern instruments this is done by using suitable monochromators. The sample is taken in quartz cuvettes, though for visible region even glass cells can be used. The detection of the transmitted radiation is done generally by a phototube or a photomultiplier tube. Nowadays, the modern machines employ diode arrays for detection purposes. These components are assembled into single beam, double beam and diode array spectrometers [69].

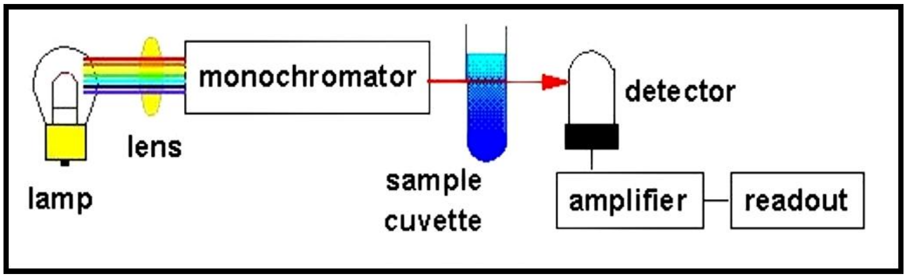

Figure 3.13: Schematic of a single beam uv-vis spectrophotometer

The UV-Visible spectrophotometer uses two light sources as illustrated in figure 3.14, a deuterium (D_2) lamp for ultraviolet light and a tungsten (W) lamp for visible light. After bouncing off a mirror (mirror 1), the light beam passes through a slit and hits a diffraction grating. The grating can be rotated allowing for a specific wavelength to be selected. At any specific orientation of the grating, only monochromatic (single wavelength) successfully passes through a slit. A filter is used to remove unwanted higher orders of diffraction. The light beam hits a second mirror before it gets split by a half mirror (half of the light is reflected, the other half passes through). One of the beams is allowed to pass through a reference cuvette (which contains the solvent only), the other passes through the sample cuvette. The intensities of the light beams are then measured at the end [70].

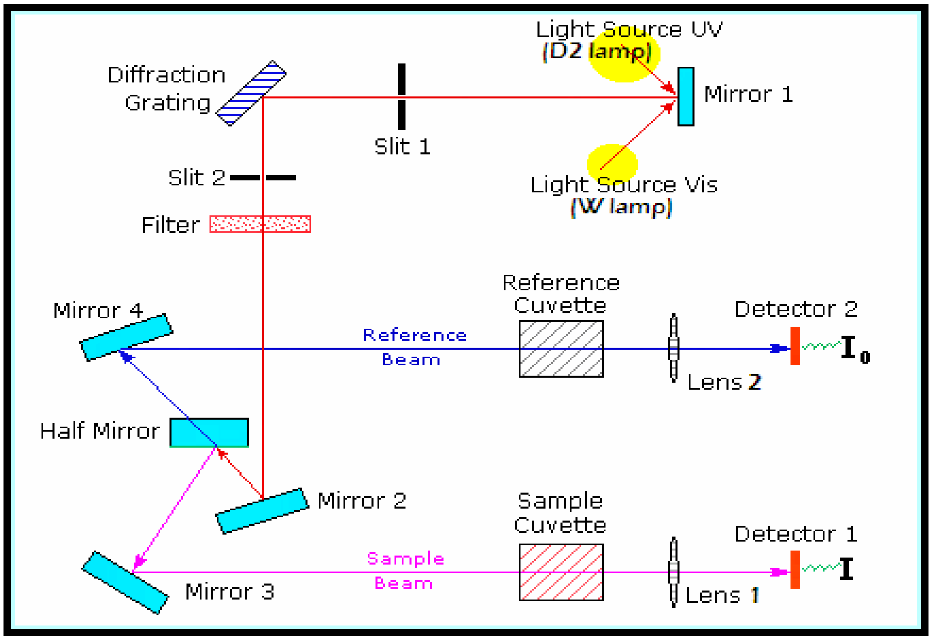

Figure 3.14: Working of a uv-vis spectrophotometer

In a typical absorption spectral measurement a monochromatic radiation is made to fall on a sample taken in suitable container called **cuvette**. In such a situation a part of the radiation is reflected, a part is absorbed, and a part is transmitted.

Bouguer's law or **Lambert's law** expresses the relationship between the light absorption capacity of the sample and the thickness of the absorbing medium; and **Beer's law**, which expresses the relationship between the light absorptive capacity of the sample and its concentration. The two laws are combined together to give **Beer-Lambert's law**.

3.4.6.3 Ideal uses of UV-VIS Spectroscopy

- Detection of Impurities
- UV absorption spectroscopy can be used for the quantitative determination of compounds that absorb UV radiation

- Kinetics of reaction can also be studied using UV spectroscopy. The UV radiation is passed through the reaction cell and the absorbance changes can be observed [71].

3.4.7 Current density-voltage (J-V) characteristics

The electrical characteristics of photovoltaic (PV) devices are depicted by current-voltage (*I-V) curves*. These I-V curves are obtained by exposing the cell to a constant level of light, varying the resistance of the load, and measuring the current that is produced. The conversion efficiency of a solar cell is the percentage of the solar energy shining on it that is converted into electrical energy [72]. In the present study, J-V characteristics were measured using Source Meter interfaced with computer under the illumination of simulated sunlight (Solar Simulator).

3.4.7.1 Principle of I-V characterization

I-V curves represent the most important and direct characterization method for solar cells. The open circuit voltage (Voc), short circuit current (Isc) and the fill factor of the I-V curve determines the efficiency (η) of DSSC. Short-circuit current density (J_{SC}) is short-circuit current per active area [73]. To remove the dependence of the solar cell area, the short-circuit current density is listed rather than the short-circuit current. Fill factor describes how well the area under the I-V curve "fills in" the maximum possible rectangle defined by $J_{SC} \times V_{OC}$. The fill factor can be visualized by the ratio of the areas of the A and B in figure 3.15.

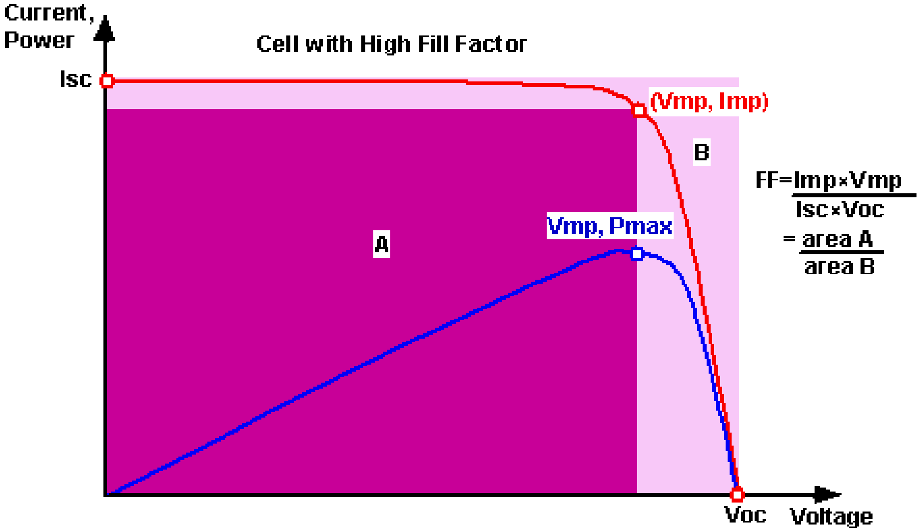

Figure 3.15: Graph of cell output current (red line) and power (blue line) as function of voltage. I_{SC}, V_{OC} and the maximum power points ($V_{mp} \times I_{mp}$) are indicated

3.4.7.2 Determining the parameters of solar cell

On an I-V plot, the vertical axis refers to current, and the horizontal axis refers to voltage. The actual I-V curve typically passes through two significant points:

- The *short-circuit current density* (J_{SC}) is the current produced when the positive and negative terminals of the cell are short-circuited and the voltage between the terminals is zero, which corresponds to a load resistance of zero.
- The *open-circuit voltage* (V_{OC}) is the voltage across the positive and negative terminals under open-circuit conditions when the current is zero, which corresponds to a load resistance of infinity.

The cell may be operated over a range of voltages and currents. By varying the load resistance from zero (a short circuit) to infinity (an open circuit), the highest efficiency as the point at which the cell delivers maximum power, can be determined. That power is the product of voltage times current. Therefore, on the I-V curve, the *maximum-power point* (P_{max}) occurs where the product of current times voltage is a maximum. That point represents the maximum efficiency of the solar device at converting sunlight into electricity [72]. The efficiency and fill factor of the solar cells is calculated using the following equations:

$$\eta(\%) = \frac{J_{SC} \times V_{OC} \times FF}{P_{in}} \tag{3.4}$$

$$FF = \frac{P_{max}}{J_{SC} \times V_{OC}} \tag{3.5}$$

4.1 X-ray diffraction analysis

X-ray diffraction patterns were recorded by an X-ray diffractometer (PANalytical X'Pert PRO MRD) using CuKα radiation (λ= 1.54060A˚) with radiation operated at 45kV and 40mA. Figure 4.1 shows the XRD spectra obtained from TiO_2, TiTb1, TiTb5 and TiTb10 samples.

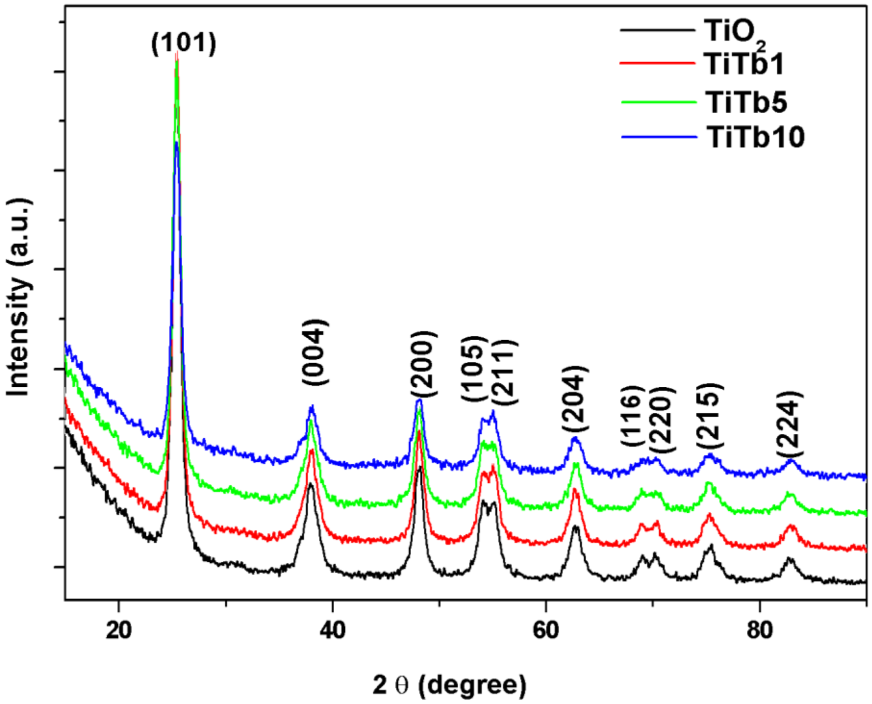

Figure 4.1: X-ray diffraction patterns of TiO_2, TiTb1, TiTb5, and TiTb10

The diffraction peak positioned at values 2θ values of 25.32°, 37.84°, 48.07°, 53.95°, 55.10°, 62.75°, 68.84°, 70.34°, 75.12°, 82.75° corresponds to the (101), (004), (200), (105), (211), (204), (116), (220), (215), (224) planes matches well with anatase structured TiO_2 with tetragonal phase compared with JCPDS (File no. 84-1286). The peak position of mixed oxides was nearly same as pure mesoporous TiO_2, thereby implying both contain the crystallized anatase phase. However, the broadness of the peak became larger as more Tb_2O_3 was incorporated.

The average crystallite sizes were determined by Scherrer's formula [74] (equation 1), as given below:

$$d = \frac{k\lambda}{\beta \cos \Theta} \tag{4.1}$$

where d is the crystallite size, *k* is the shape factor (*k* = 0.94), λ is the x-ray wavelength (1.54Å), θ is the diffraction angle, β is the line broadening at half the maximum intensity (FWHM). Table 4.1 shows the crystallite size obtained from the Scherrer's formula for all the samples.

Table 4.1: Crystallite size calculated from the XRD pattern using Debye–Scherer formula

Sample	FWHM	2θ	D (nm)
TiO_2	0.84	25.37	9.65
TiTb1	0.80	25.39	10.11
TiTb5	0.80	25.38	10.12
TiTb10	0.86	25.39	9.46

The crystallite size calculated using Scherrer's equation has been found to be about 9.65, 10.11, 10.12 and 9.46 nm for TiO_2, TiTb1, TiTb5 and TiTb10 respectively. The data obtained from the Scherer's equation shows a slight increase in crystallite size with increase in Tb_2O_3 content. The Tb_2O_3 coating influences the lattice structure and the crystallite size.

4.2 Transmission electron microscopy

TEM micrographs of TiO_2 and TiTb1 nanoparticles are shown in figure 4.2. The average particle size of the bare TiO_2 and TiTb1 nanoparticles has been found to be, 9.3 nm and 10.1 nm, respectively.

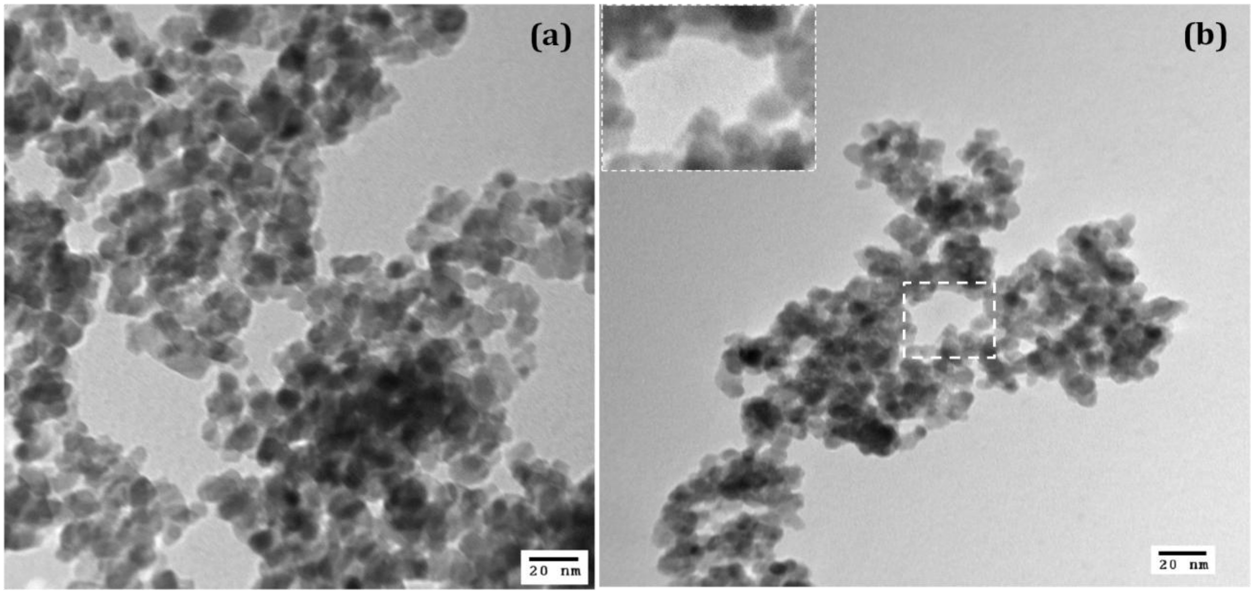

Figure 4.2: TEM images of (a) TiO_2 (b) TiTb1 nanoparticles. The inset in figure (b) shows the magnified view of the dotted square

4.3 Energy dispersive x-ray spectroscopy

Energy dispersive x-ray spectroscopy (EDAX) spectrum of TiTb1 sample has been shown in figure 4.3. The EDAX spectrum shows distinct peaks of O, Ti and Tb with atomic percentage 68.81, 30.62 and 0.57, respectively, concluding stoichiometric formation of TiTb1 sample. The analysis of EDAX spectrum concludes that the surface of TiO_2 contains Tb and O, which confirms the formation of Tb_2O_3 coating on the surface of TiO_2 nanoparticles.

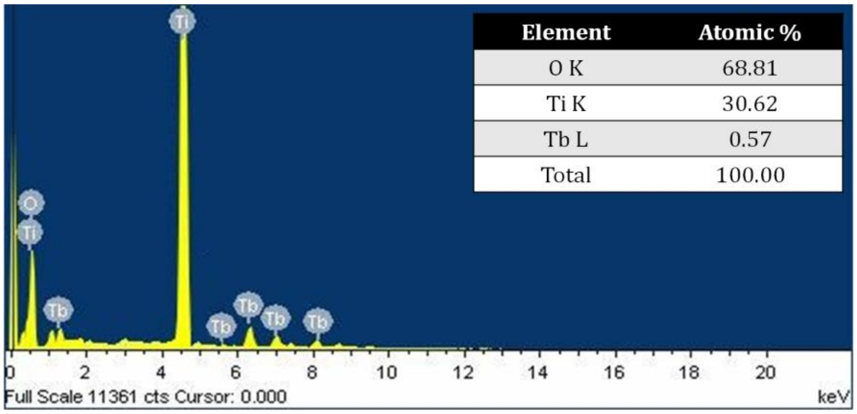

Element	Atomic %
O K	68.81
Ti K	30.62
Tb L	0.57
Total	100.00

Figure 4.3: EDAX spectrum of TiTb1 sample

4.4 Fourier Transform Infrared Spectroscopy

The Fourier transform infrared (FTIR) spectra reveal absorption peaks, corresponding to the vibration modes of hydroxyl, carboxylate, and alkane groups in the synthesized samples. Figure 4.4 presents the FTIR spectra of TiO_2, TiTb1, TiTb5, TiTb10 nanoparticles. The spectra displays a broad absorption peak around 3,428 cm^{-1} assigned to the stretching vibration of -OH group on the TiO_2 surface. This is because the hydroxyl group and adsorbed water dominate the surface chemistry of TiO_2. Small peaks at 2,847 and 2,920 cm^{-1} are due to C–H stretching vibration of alkane groups. The peak observed at 1,632 cm^{-1} has been assigned to the bending modes of the adsorbed water [75]. The characteristic vibrations of the inorganic Ti-O stretch have been observed in the range 400-900 cm^{-1}. The peak at 1374 cm^{-1} has been assigned to sulphate group. The peak observed at 1117 cm^{-1} is due to the plane bending vibrations of C-H mode.

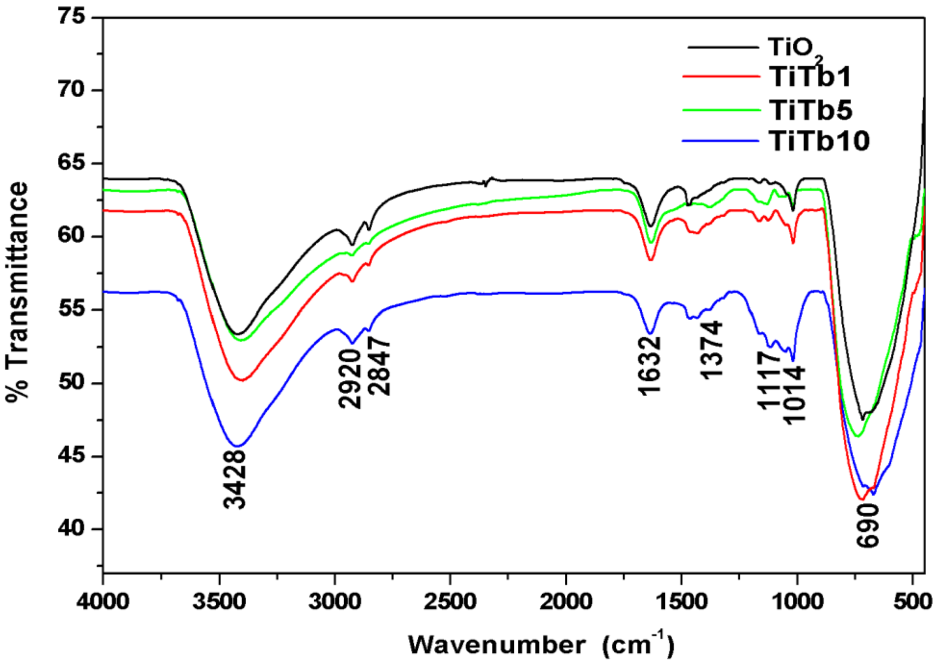

Figure 4.4: FTIR spectra of TiO_2, TiTb1, TiTb5 and TiTb10 samples

4.5 Photoluminescence spectroscopy

PL spectroscopy was performed in order to analyze the phenomenon of electron–hole recombination process taking place in the bare and Tb_2O_3/TiO_2 nanoparticles. Figure 4.5 shows the PL spectra of the synthesized samples. In the PL spectrum of bare TiO_2 nanoparticles, the emission signal at 485 nm is attributed to the charge-transfer from Ti^{3+} to oxygen anion in a TiO_6^{8-} complex, related with oxygen vacancies at the TiO_2 surface [76]. The emission peak at 383 nm corresponds to a direct band emission—the fundamental band gap of 3.2 eV of anatase TiO_2 [77]. The peak observed around 421 nm is attributed to the self-trapped excitons [78]. The emission peak at 444 nm is associated with the emission process related to the presence of oxygen vacancy defects in TiO_2. The green emission, 529 nm, can be associated with anion vacancies on the surface of TiO_2 nanoparticles [79].

On exciting the Tb_2O_3/TiO_2 nanoparticles at 325 nm, the Tb^{3+} ions give emission at 447 nm and 461 nm corresponding to $^5D_3$-$^7F_5$ transitions [80]. It is well known that, the emission transitions of Tb^{3+} ions are mainly from the two excited energy levels $^5D_3$ and $^5D_4 \rightarrow {}^7F_J$ ground states because the large energy gap between $^5D_3$, $^5D_4$ states and ^7F_J ground states causes the relaxation process from these two ($^5D_3$ and $^5D_4$) excited energy states to the ^7F_J ground states and this occurs radiatively and spectra in the visible region is obtained. Further the spectral distribution mainly depends on the concentration of Tb^{3+} ions [81-83].

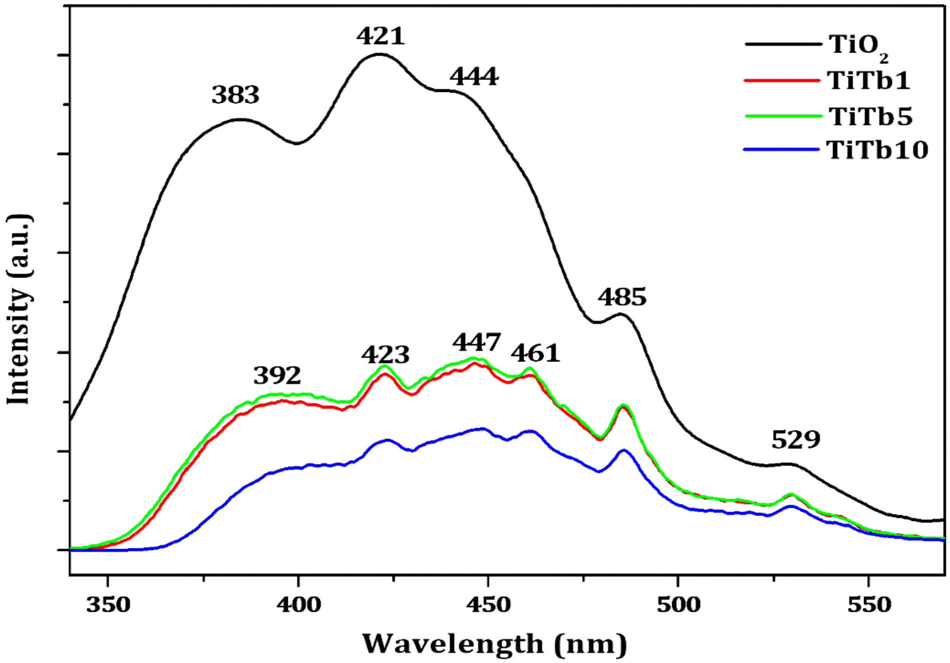

Figure 4.5: Photoluminescence spectra of TiO_2, TiTb1, TiTb5 and TiTb10 nanoparticles

As the concentration of Tb^{3+} ions increases, the distance between the ions decreases and they come closer to each other. This leads to the transfer of energy between terbium ions and then this energy is released through some non-radiative processes [84]. A wide band in the 400–500 nm region related to anatase TiO_2 is also observed.

It has been observed from the PL analysis that Tb_2O_3/TiO_2 nanoparticles give emission having lower intensity compared to the bare TiO_2 nanoparticles. Generally, PL emission intensity increases with the increasing number of emitted electrons resulting from recombination between excited electrons and holes, and, consequently, decreasing the photoactivity [85]. Tb_2O_3 coating on TiO_2 nanoparticles has reduced the unwanted non-radiative decay pathways, thus increasing the electron injection efficiency. The decrease in intensity of PL, infers that Tb_2O_3 coating on TiO_2 suppresses the electron–hole recombination process on TiO_2 surface. The strong quenching of photoluminescence is due to the increase in the separation efficiency of the photogenerated electron–hole pairs. This enhances the transferring process to the FTO, leading to easier electron transfer activities. Therefore, it can be anticipated that the performance of DSSC, fabricated using Tb_2O_3/TiO_2 nanoparticles, is likely to be better than that of bare TiO_2 DSSC.

4.6 Dye desorption analysis

Procedure for dye desorption: The influence of Tb_2O_3 coating on dye adsorption has been investigated by measuring the absorption spectra of the N719 dye desorbed from the fabricated electrodes. To desorb the dye molecules from the electrodes, they were soaked in 0.1 mM aqueous NaOH solution.

Figure 4.6 shows the UV–Visible absorption spectra of the N719 dye desorbed from the electrodes. The peaks observed at 380 nm and 515 nm correspond to the characteristic absorption of N719 dye. The intensity of the UV-visible absorption is proportional to the degree of dye adsorption on the electrode. From the absorption study, it has been found that the amount of dye adsorbed on the TiTb1 electrode show enhanced dye adsorption as compared to the TiO_2 electrode.

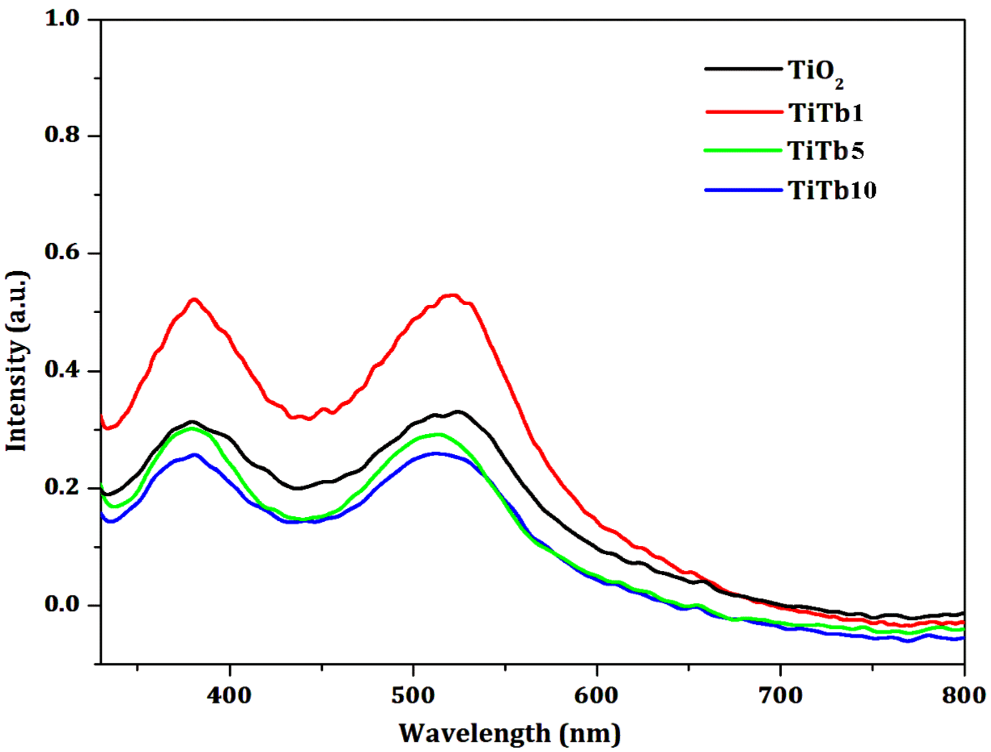

Figure 4.6: UV–visible absorption spectra of the N719 dye desorbed from TiO_2, TiTb1, TiTb5 and TiTb10 electrode

Figure 4.6 illustrates that the electrode fabricated from TiTb1 sample shows maximum photon capturing in the visible region and furthermore indicate strong light-harvesting capacity. The enhanced adsorption of the dye molecules on TiTb1 based electrode improves the DSSC performance, as this increases the concentration of photogenerated electrons by visible light [86]. For the generation of high photocurrent density, the amount of dye adsorbed on nanocrystalline film should be high. The decrease in the adsorbed dye from TiTb5 and TiTb10 electrodes is due to the decrease in the surface area of the working electrodes due to high concentration of coating precursor. The photocurrent of DSSC is influenced by the initial number of photogenerated electron–hole pairs, which depend on the film structure of the electrodes.

4.7 Photocurrent density–voltage (J–V) characteristics

Figure 4.7 shows the J–V curves obtained from DSSC fabricated using TiO_2, TiTb1, TiTb5 and TiTb10 nanoparticles, with an active area of 1 x 1 cm^2. The various parameters (J_{SC}, V_{OC}, fill factor (FF) and efficiency (η)) calculated from J–V curve are summarized in Table 1. The fill factor and efficiency of the DSSCs have been calculated using the following equations:

$$FF = \frac{P_{max}}{J_{SC} \times V_{OC}} \tag{4.2}$$

$$\eta = \frac{J_{SC} \times V_{OC} \times FF}{P_{in}} \tag{4.3}$$

where P_{max} is the maximum power and P_{in} is the power of the input light.

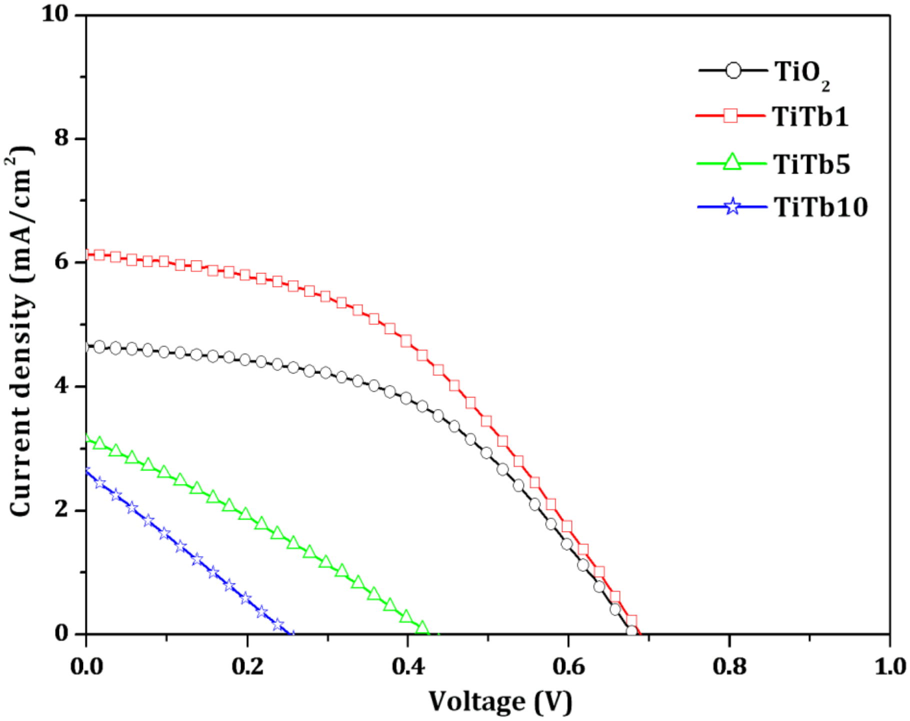

Figure 4.7: J–V curves of TiO_2, TiTb1, TiTb5 and TiTb10 based DSSCs

An increase in the parameters has been registered in DSSC fabricated from TiTb1 nanoparticles compared to bare TiO_2 nanoparticles. This increase can be explained as follows: The coating Tb_2O_3 on TiO_2 acts as an energy barrier, which minimizes the e^-/h^+ recombination and retards the back electron transfer to the electrolyte, resulting in increase in the value of open circuit voltage from 681 to 696 mV in case of TiO_2 DSSC and TiTb1 DSSC, respectively. The increase in Voc indicates the Tb_2O_3 coating on TiO_2 nanoparticles has decreased the recombination rate of the electron to the electrolyte [87].

Table 4.2: Photovoltaic parameters as obtained from the J–V curve

Sample name	J_{SC} (mA/cm^2)	V_{OC} (mV)	FF	Efficiency (η)
TiO_2	4.66	681	0.48	1.54
TiTb1	6.13	696	0.44	1.88
TiTb5	3.16	421	0.29	0.38
TiTb10	2.61	250	0.25	0.16

An increase in the short circuit current density from 4.66 mA/cm^2 for TiO_2 DSSC to 6.13 mA/cm^2 for TiTb1 DSSC has been observed. This increase in short circuit current density can be explained by the fact that the amount of dye molecules adsorbed on Tb_2O_3/TiO_2 electrode is higher than the bare TiO_2 electrode (figure 4.6) [88]. The higher extent of absorption of dye molecules in case of Tb_2O_3/TiO_2 leads to higher JSC, which results in greater light harvesting efficiency, and, hence, improves the performance of DSSC [89]. The enhancement of V_{OC} and J_{SC} in the case of TiTb1 DSSC as compared to TiO_2 DSSC leads to an increase in the overall efficiency from 1.54% to 1.88%. However, TiTb5 and TiTb10 based DSSC show a decline in efficiency as compared to TiTb1 based DSSC. This is due to the fact that thicker coating more effectively reduces the charge recombination but it also reduces the rate of electron injection into TiO_2 [90]. With the increased distance for electrons to tunnel through the Tb_2O_3 coating to TiO_2, J_{SC} has decreased due to a reduced interfacial charge transfer rate. The enhancement of the cell parameters (V_{OC}, J_{SC}, FF) lead to an increase in the overall DSSC efficiency.

CHAPTER-5 Conclusions

The aim of the present research was to synthesize Tb_2O_3 coated TiO_2 nanoparticles as electrode material for dye sensitized solar cells. The structural, morphological and optical of the nanoparticles were investigated. J-V characteristics of the fabricated DSSCs were also analysed. Following are the conclusions of the work performed:

- Synthesis of bare TiO_2 nanoparticles has been done by sol-gel method and the Tb_2O_3 coating has been done by hydrothermal process.

- From XRD analysis, all the peaks are indexed and well-matched to the tetragonal structure having anatase phase (JCPDS Card No. 841286) of TiO_2.

- The EDAX spectrum shows that the surface of TiO_2 contains Tb and O, which confirms the formation of Tb_2O_3 coating on the surface of TiO_2 nanoparticles.

- From the TEM micrographs, the particle size of TiO_2 and Tb_2O_3/TiO_2 nanoparticles has been found to in the range of 9.3 nm and 10.1 nm respectively.

- The photoluminescence analysis of bare and coated showed that the Tb_2O_3 coating leads to reduction of the unwanted non-radiative decay pathways, thus increasing the electron injection efficiency from TiO_2 to FTO.

- From the dye desorption studies, it has been found that the amount of dye adsorbed on the TiTb1 photoelectrode is higher than that of bare TiO_2 electrode.

- DSSC fabricated using Tb_2O_3/TiO_2 nanoparticles as electrode; exhibit higher conversion efficiency, 1.88%, as compared to that of the bare TiO_2 nanoparticles, 1.54%. Coating of Tb_2O_3 on TiO_2 nanoparticles acts as an energy barrier, minimizes the electron–hole recombination at the TiO_2/dye/electrolyte interface by increasing the surface resistance of Tb_2O_3 modified TiO_2 and retarding the back electron transfer to the electrolyte; this, in turn, increases V_{OC}. Also, the coating leads to an increase in the dye adsorption, which leads to greater light harvesting efficiency, and, hence leads to increase in J_{SC}. The improvement in DSSC efficiency has been attributed to the enhanced dye adsorption as well as retardation of the back electron transfer. Therefore from the present study, it is concluded that coating of higher band gap materials on TiO_2 open the way to use these nanostructures in DSSCs.

References

1) Lee, J.J., Rahman, M.M., Sarker, S., Nath, N.C.D., Ahammad, A.J.S., Lee, J. K., Metal Oxides and Their Composites for the Photoelectrode of Dye Sensitized Solar Cells, Advances in Composite Materials for Medicine and Nanotechnology, 978-953-307-235-7, 2011
2) Gratzel, M., Acc Chem Res. ,42(11), 1788-98, 2009
3) Crabtree, G.W., Lewis, N. S., Physics today, 60(3), 37-42, 2007
4) http://org.ntnu.no/solarcells/pages/generations.php
5) http://www.irena.org/DocumentDownloads/Publications/RE_Technologies_Cost_Analysis-SOLAR_PV.pdf
6) Chapin, D., Fuller, C., Pearson, G., J. Appl. Phys., 25, 676–677, 1954
7) Goetzberger, A., Luther, J., Willeke, G., Sol. Energy Mater. Sol.Cells, 74 (1–11), 2002
8) Carlson, D., Wronski, C., Appl. Phys. Lett., 28, 671–673, 1976
9) Cusano, D., Solid-State Electron., 6, 217–218, 1963
10) Morgan, D., Shines, C., Jeter, S., Blazka, M., Elwell, M., Wilson, R., Ward, S., Price, H., Moskowitz, p., Toxicol. Appl. Pharmacol., 147, 399–410, 1997
11) Cho, S., Maysinger, D., Jain, M., Roder, B., Hackbarth, S., Winnik, F., Langmuir, 23, 1974–1980, 2007
12) Kazmerski, L., White, F., Morgan, G., Appl. Phys. Lett., 29, 268–270, 1976
13) Dimmler, B., and Schock, H.W., Prog. Photovoltaics Res. Appl., 4, 425–433, 1996
14) Green, M., Emery, K., Hishikawa, Y., Warta, W., Prog.Photovoltaics Res. Appl., 16, 435–440, 2008.
15) Gunes, S., Neugebauer, H., Sariciftci., N.S., Chem. Rev., 107(4)1324-1338, 2007
16) Luo, J., Wu, H., He, C., Li, A., Yang, W., Cao, Y., Appl. Phys. Lett., 95, 043301, 2009
17) Tulloch, G., J. Photochem. Photobiol., A, 164, 209–219, 2004
18) Otaka, H., Kira, M., Yano, K., Ito, S., Mitekura, H., Kawata, T., Matsui, F., J. Photochem. Photobiol., A, 164(6–3), 2004
19) Gratzel, M., Inorg. Chem., 44, 6841–6851, 2005
20) B, O.R., Gratzel, M., Nature, 353, 737-740, 1991
21) http://hdl.rutgers.edu/1782.1/rucore10001600001.ETD.000063317

22) Gratzel, M., Journal of Sol-Gel Science and Technology, 22(1-2), 7-13, 2001.

23) Lee, J .K.,Yang, M., J. Materials Sciences and Engineering : B,176(15), 1142-1160, 2011

24) Hardin, B. E., Snaith, H. J., McGehee, M.D., Nature Photonics, 6(3), 133–135, 2012.

25) Zhang, Q., Cao, G., Nano Today, 6(1), 91-109, 2011

26) Kim, S.S., Yum, J.H., Sung, Y.E., J. Photochem. Photobiol. A Chem. 171(3), 269-273, 2005

27) Bisquert, J., Cahen, D., Hodes, G., Ru1hle, S., Zaban., A.,J. Phys. Chem. B, 108, 24, 2004

28) Yu, H, Xue, B., Liu, P., Qiu, J., Wen, W., Zhang, S., Zhao, H., ACS Appl. Mater. Interfaces 4(3), 1289, 2012

29) Law, M., Greene, L.E., Radenovic, A., Kuykendall, T., Liphardt, J., Yang, P., J. Phys. Chem. B., 110(45), 22652–22663, 2006

30) Kaur, M., Verma, N. K., J Mater Sci: Mater Electron, 2013, DOI: 10.1007/s10854-013-1293-0

31) Li, Q., Lin, J., Wu, J., Lan, Z., Wang, Y., Peng, F., Huang, M., Journal of Luminescence, 134, 59-62, 2013

32) Wu, J., Xie, G., Lin, J., Lan, Z., Huang, M., Huang, Y., Journal of Power Sources, 195(19), 6937-6940, 2010

33) Wang, X., Yang, Y.L., Wang, P., Li, L., Fan, R.Q., Cao, W.W., Yang, B., Wang, H., Liu, J.Y., Dalton Trans., 41, 10619-10625, 2012

34) Xie, G., Wu, J., Lin, J., Li, Q., Lan, Z., Xiao, Y., Yue, G., Ye, H., Huang, M., Energy Sources, Part A: Recovery, Utilization, and Environmental Effects, 34(16), 1534-1540, 2012

35) Lu, L., Li, R., Peng, T., Fan, K., Dai, K., Renew. Energy, 36(12), 3386-3393, 2011

36) Yahav, S, Ruhle, S., Greenwald, S., Barad, H.N., Shalom, M., Zaban, A., J. Phys. Chem. C, 115(43), 21481–21486, 2011

37) Yu, H., Xue, B., Liu, P., Qiu, J., Wen, W., Zhang, S., Zhao, H., ACS Appl. Mater. Interfaces, 4 (3),1289–1294, 2012

38) Zhang, J., Peng, W., Chen, Z., Chen, H., Han, L., J. Phys. Chem. C, 116 (36), 19182–19190, 2012
39) Zalas, M., Klein, M., Int. J. Photoenergy , 2012 , 927407(8), 2012
40) Jian, Y., Limei, P., Xiangxin, X., Mei, W., Tai, Q., Journal of Rare Earths, 27(2), 204-210, 2009
41) Choi, H., Kim, J.H., Yi, S.S., Moon, B.K., Jeong, J.H., Journal of Alloys and Compounds, 408-412, 816-819, 2006
42) Moon, B.K., Jeong, J.H., Yi, S.S., Choi, S.E., Kim, P.S., Choi, H., Kim, J.H., Journal of Luminescence, 122-123, 873-875, 2007
43) Wakefield, G., Keron, H.A., Dobson, P.J., Hutchison, J.L., Journal of Physics and Chemistry of Solids, 60(4), 503-508, 1999
44) Macwan, D. P., Dave, P. N., Chaturvedi, S., J Mater Sci, 46(11), 3669–3686, 2011
45) Feng, S., Xu, R., Accounts of Chemical Research, 34(3), 239–247, 2001
46) Xu, R., Pang, W, Huo, Q., Modern Inorganic Synthetic Chemistry, 78, 2010
47) Tanner, B.K., Hsea, T.B.A., Clarke, J., Pape, I., Bassi, A.L., Fulthorpe, B.D., Applied surface science 182, 202-208, 2001
48) http://www.terrachem.de/roentgenbeugungsanalyse.php?language=en
49) http://emsiteacherworkshop.stanford.edu/pages/workshopresources/XRDSEM%20tutorial.doc
50) http://nanoscience.skku.edu/index.php?cont=research&subcont=characterization
51) http://www.eaglabs.com/mc/x-ray-diffraction.html
52) http://www.hk-phy.org/atomic_world/tem/tem04_e.html
53) httpwww.nobelprize.orgeducationalphysicsmicroscopestemindex.html
54) http://portal.tugraz.at/portal/page/portal/felmi/research/TEM%20and%20Nanoanalysis/Principles%20of%20TEM
55) http://www.tutorsglobe.com/homework-help/botany/transmission-electron-microscopy-73287.aspx

56) http://classroom.sdmesa.edu/eschmid/Lecture2-Microbio.htm

57) http://www.eaglabs.com/mc/scanning-transmission-electron-microscopy.html

58) http://www.aspexcorp.com/solutions/omegamax/edxspectroscopy.aspx

59) http://www.engr.sjsu.edu/MC2/SOP_EDAX.pdf

60) http://www.globalsino.com/micro/1/micro9999.html

61) http://www.biocenter.helsinki.fi/bi/biophys/methods_ftir.html

62) http://www.newport.com/Introduction-to-FTIRSpectroscopy/405840/1033/content.aspx

63) http://chemwiki.ucdavis.edu/Physical_Chemistry/Spectroscopy/Vibrational_Spectroscopy/Infrared_Spectroscopy/How_an_FTIR_Spectrometer_Operates

64) Leclerc, D.F., Encyclopedia of Analytical Chemistry, R.A. Meyers (Ed.), 8361–8388

65) http://www.physik.uniwuerzburg.de/EP3/Arbeitsgruppen/Optische_Spektroskopie/PL/methods.html

66) http://www.lpa.ens.fr/spip/spip.php?article266

67) http://www.itst.ucsb.edu/~vinhnguyen/Time-Frequency_Spectroscopy.ht

68) http://nsdl.niscair.res.in/handle/123456789/772

69) http://vedyadhara.ignou.ac.in/wiki/images/0/01/Unit_2_UV-Visible_Spectrometry.pdf

70) http://bouman.chem.georgetown.edu/S00/handout/spectrometer.htm

71) http://www.pharmatutor.org/pharma-analysis/analytical-aspects-of-uv-visible-spectroscopy/applications.html

72) http://www.eere.energy.gov/basics/renewable_energy/pv_cell_conversion_efficiency.htm

73) http://www.dyesol.com/media/wysiwyg/Documents/dsc-resourcelibrary/What_Physical_Factors_Affect_Current-Voltage_Characteristics_of_Dye_Solar_Cells-Dyesol-HansDesilvestro -2008.pdf

74) Debye, P., Rontgenstrahlen, Z. V., Annalender, P., 351, 809, 1915

75) Beydoun, D., Amal, R., Materials Science and Engineering B, 94 (1), 71-81, 2002

76) Liu, V., Li, V., Sedhain, A., Lin, J., Jiang, V., J. Phys.Chem. C, 112, 17127, 2008

77) Chaveanghong, S., Smith, S.M., Sudchanham, J., Amornsakchai, T., J. Microsc. Soc. Thail., 4, 36, 2011

78) Song, X., Gao, L., Langmuir, 23, 11850, 2007

79) Jun, J., Jin,C ., Kim, H., Kang, J., Lee, C., Appl. Phys. A, 96 , 813, 2009

80) Sontakke, A.D., Biswas,K., Annapurna, K., Journal of Luminescence, 129(11), 1347-1355, 2009

81) Liao, J., Qiu, B., Wen, H., You, W., Xiao, Y., J Lumin, 130(5), 762-766, 2010

82) Singh, V., Watanabe, S., GunduRao, T.K., Kwak, H.Y., Solid State Sci, 12, 1981, 2010

83) Zhang, F., Wang, Y., Liu, B., Wen, Y., Tao, Y., Mater Res Bull, 46:722, 2011

84) Mari, B., Singh, K.C., Sahal, M., Khatkar, S.P., Taxak, V.B., Kumar, M., J Lumin, 130 (11), 2128-2132, 2010

85) Wang, D., Xue, G., Zhen, Y., FLiD, F., J Mater Chem, 22, 4751-4758, 2012

86) Cho, T.Y, Han, C.W., Jun, Yoon, S.G., Scientific Reports, 3, 1496, 2013

87) Ramar, A., Soundappan, T., Chen, S.M., Rajkumar, M., Ramiah, S., Int. J. Electrochem. Sci., 7, 11734, 2012

88) Kuo, C.G., Yang, C.F., Hwang, L.R., Huang, J.S., Int. J. Photoenergy, 2013, 650973, 2013

89) Kim, M.H., Kwon, Y.U., J. Phys. Chem. C, 113, 17176, 2009

90) Menzies, D.B., Dai, Q., Bourgeois, L., Caruso, R.A., Cheng, Y.B., Simon, G.P., Spiccia, L., Nanotechnology, 18, 125608, 2007